Inward buckling of spiral layered structures subject to volumetric expansion and external constraint

Xinran Shi, Juner Zhu

[a]*Department of Mechanical and Industrial Engineering, Northeastern University, 360 Huntington Ave, Boston, 02115, MA, USA*

Abstract

Spiral layered structures subjected to thermal or diffusion-induced expansion often develop inward collapse, yet predictive models that connect geometry, confinement, and contact remain limited. Here we formulate a planar beam-based theory for an Archimedean spiral confined by a rigid circular ring, in which eigenstrain is converted into compressive circumferential resultants through kinematic constraint and unilateral contact. Using a variational framework, we derive spiral-path Föppl–von Kármán–type governing equations including a one-sided Winkler penalty representation of wall contact. A Rayleigh–Ritz energy estimate is then used to obtain closed-form scaling relations for the onset of instability. As an analytical benchmark, we reduce the spiral to the zero-pitch limit and recover a circular ring model, yielding mode-dependent critical compressive resultants for detached and fully contacting pre-buckling states. Complementary Dynamic/Explicit finite-element simulations under prescribed thermal expansion validate the theory and provide robust onset identification via internal-energy release, kinetic-energy bursts, and Fourier-mode growth. Finally, we study physically realistic multi-turn spirals, where turn-to-turn self-contact produces intrinsic kinematic locking without artificial end constraints, and we nondimensionalize the parameter space using the inner radius as the reference length to characterize the response in terms of thickness and turn number. The results establish a unified eigenstrain-to-compression mechanism for inward buckling, quantify the roles of confinement and contact state, and provide dimensionless design trends for layered spiral structures.

Keywords: Archimedean spirals, layered structures, volumetric expansion, Rayleigh–Ritz method, buckling instability

Table 1: Notation: geometry and kinematics.

Symbol	Definition
r_0	Initial (inner) radius at $\theta = 0$; reference length for nondimensionalization.
r_{out}	Outer radius of the spiral.
R	Radius of the circular ring in the ring-reduction limit ($D \to 0$).
θ	Polar angle parameter along the spiral/ring.
s	Arc-length coordinate; $ds = J(\theta)\, d\theta$.
$J(\theta)$	Jacobian: $J = \sqrt{r^2 + (dr/d\theta)^2}$.
$r(\theta)$	Spiral centerline radius; Archimedean: $r = r_0 + b\theta$.
D	Radial increment per full turn (2π) of the spiral.
b	Spiral slope parameter, $b = D/(2\pi)$.
N_t	Number of turns.
t	Layer thickness (self-contact multi-turn: $D = t$).
$u(\theta)$, $w(\theta)$	Tangential and outward-normal displacements of the centerline.
Sign of w	$w > 0$ outward (toward rigid wall / penetration direction in penalty contact).
$\kappa(\theta)$	Reference curvature; for a ring $\kappa = 1/R$.
$\tilde{\kappa}(\theta)$	Deformed curvature; $\Delta\kappa = \tilde{\kappa} - \kappa$.

Table 2: Notation: mechanics, contact, and nondimensional groups.

Symbol	Definition
E	Young's modulus.
A, I	Area $A = bh$ (out-of-plane thickness $b = 1$) and second moment of area of the beam's cross section $I = bh^3/12$.
EA, EI	Extensional and bending stiffness.
ε_{tt}	Tangential (Green–Lagrange) strain along the centerline.
$\varepsilon_{tt}^{\text{eigen}}$	Eigenstrain: $\alpha_{\text{eff}}\Delta T(\theta)$ or $\beta_{\text{eff}}\Delta c(\theta)$.
$\varepsilon_{tt}^{\text{elastic}}$	Elastic strain: $\varepsilon_{tt} - \varepsilon_{tt}^{\text{eigen}}$.
N	Tangential resultant, $N = EA\,\varepsilon_{tt}^{\text{elastic}}$ (positive in tension).
M	Bending moment, $M = EI(\tilde{\kappa} - \kappa)$.
Q	Shear resultant: $Q = \frac{1}{J}(M_{,\theta} - Nw_{,\theta})$.
$H(\cdot)$	Heaviside function (unilateral contact activation).
k, k_w	Wall penalty stiffness (one-turn rigid-ring contact).
k_N	Inter-layer normal penalty stiffness (turn-to-turn contact).
$g(\theta)$	Inter-layer gap (negative: overclosure).
$g_w(\theta)$	Wall gap to rigid ring (negative: overclosure).
α_{eff}, β_{eff}	Effective thermal / chemical expansion coefficients.
$\Delta T(\theta)$, $\Delta c(\theta)$	Prescribed temperature / concentration change.
ε_{cr}	Critical eigenstrain: $\Theta_{\text{cr}} = \alpha_{\text{eff}}\Delta T_{\text{cr}}$.
$\bar{(\cdot)}$	Dimensionless variable scaled by r_0 (e.g., $\bar{w} = w/r_0$).
$\hat{(\cdot)}$	Dimensionless geometry ratio (e.g., $\hat{t} = t/r_0$, $\hat{R} = R/r_0$).
$\bar{N}$	Dimensionless load: $\bar{N} = Nr_0^2/(EI)$.
$\bar{k}$	Dimensionless stiffness: $\bar{k} = kr_0^4/(EI)$.
μ	Coulomb friction coefficient (used only in the multi-layer frictional study).

1. Introduction

Spirals are ubiquitous in nature, where most follow a logarithmic form ($r = r_0 e^{k\theta}$) driven by proportional growth ($dr/d\theta \propto r$), producing the self-similar patterns seen in seashells and chameleon tails (Wentworth Thompson, 1917; Jean, 1994; Wang et al., 2025). In contrast, spirals in engineering typically arise from the rolling of sheet-like materials with constant thickness, which naturally generates an Archimedean form ($r = r_0 + b\theta$) with constant spacing between layers ($dr/d\theta \equiv b$). This geometry enables efficient packaging of long continuous sheets, as seen in sheet metal coils, battery jelly rolls (Zhu et al., 2016), roll-to-roll manufactured films (Palavesam et al., 2018), and robotic actuators (Yan et al., 2018). With the advent of advanced manufacturing, spiral architectures now extend to the microscale, forming essential components in modern electronics, including spiral inductors and interconnects in chips (Le et al., 2021).

The scientific fascination with spiral structures dates back to Archimedes, whose study of the Archimedean spiral is often regarded as a precursor to modern differential calculus (Netz, 2017). Since then, spirals have been investigated across disciplines: in biology to explain phyllotaxis and shell growth (Jean, 1994; Wentworth Thompson, 1917), and in mathematics and physics to explore the geometry and topology of two- and three-dimensional spiral forms (Polezhaev, 2019). In engineering, research on spiral mechanics has predominantly focused on manufacturing processes such as winding and rolling (Lee et al., 2012; Noh et al., 2024; Chen, 2025; Lee, 2018). Analytical and numerical models have examined the effects of winding tension, inner radius, rolling speed, and residual stress, with the objective of ensuring defect-free production. These studies have successfully optimized roll-to-roll fabrication and are now widely applied in industrial practice.

In contrast, the mechanical behavior of spiral structures during functional service remains far less understood. In many emerging applications—including batteries, microelectronic devices, and robotic systems—spiral components are subjected to cyclic volumetric expansion driven by mass diffusion, chemical reactions, thermal fluctuations, or growth processes (Li et al., 2022; Bongtae Han and Yifan Guo, 1996). Under such conditions, spirals exhibit complex deformation patterns, including inward buckling and layer-wise collapse, which can compromise structural integrity and functional

performance. Despite increasing practical relevance, a unified mechanics framework capable of describing spiral structures under internally generated expansion loads is still lacking. Understanding how distributed eigenstrains interact with geometric confinement to produce instability remains an open and fundamentally important problem. Prior studies have speculated that compressive hoop stresses in the inner layers are the primary driving force (Gelam et al., 2025; Timms et al., 2023; Gelam et al., 2024), yet existing models often approximate spirals as concentric rings or simplified shells, but these abstractions fail to reproduce the observed instability patterns. To date, no transferable theory exists to predict the onset, orientation, or progression of such instabilities.

This study presents coupled chemo-mechanical theoretical and finite element models to characterize the evolution of internal stress and buckling instabilities triggered by either solute diffusion-induced or thermal expansion. Section 2 formulates the problem and defines the geometry and mechanical setting. Section 3 establishes the kinematics and an energy-based framework for the critical buckling of the spiral structure, followed by nondimensionalization of the governing equations. The formulation is then specialized to the limiting ring case, for which an analytical solution is obtained. In Section 5, we develop finite-element models for both the spiral and the equivalent ring to compute the critical buckling load numerically. Section 5.4 presents a parametric study that quantifies how key geometric factors influence the buckling threshold. Section 6 discusses an alternative mathematical treatment of contact, compares spiral and ring predictions, benchmarks the ring solution against the classical buckling of a circular ring under external pressure, and inextensibility. Finally, Section 7 summarizes the main findings and conclusions.

2. Problem formulation

Here, we study a deformable Archimedean spiral confined by a rigid circular ring. The spiral is modeled as a slender, deformable strip of thickness h whose centerline follows an Archimedean spiral, as illustrated in Figure 2(a).

2.1. Geometry - Archimedean spiral

An Archimedean spiral is a planar curve whose radius increases linearly with the polar angle. In polar coordinates (r, θ), an Archimedean spiral can be described by the equation

$$r = r_0 + \frac{D}{2\pi}\theta, \qquad \theta \in [0,\, 2\pi N_t] \tag{1}$$

Here, r_0 denotes the initial radius (i.e., radius when $\theta = 0$). D denotes the radial increment per full turn of the spiral, corresponding to an angular change of 2π radians. For a fully-compacted spiral structure, $D = h$, the thickness of the layer. N_t represents the total number of complete turns that the spiral makes. The geometry of the Archimedean spiral is illustrated in Figure 2(a).

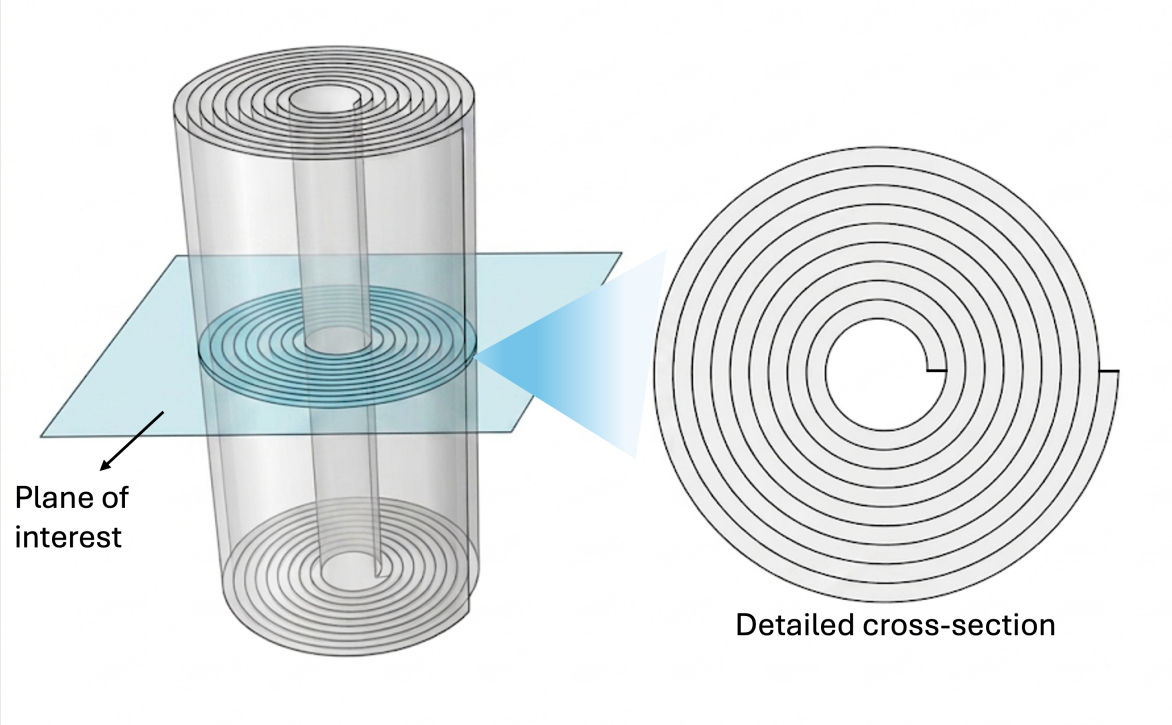

Figure 1: 3D view of the spiral-wound cylinder, highlighting the central plane of interest in light blue. The right panel shows the detailed spiral cross-section at this specific plane.

2.2. Plane strain condition assumption

In reality, spiral structures often exist in three-dimensional forms, such as battery jelly rolls or rolls of sheet metal. In this study, we focus on the cross section of a wide cylindrical roll composed of thin layers that is sufficiently far from the two edges. Under this condition, the deformation in the cross section can reasonably be assumed

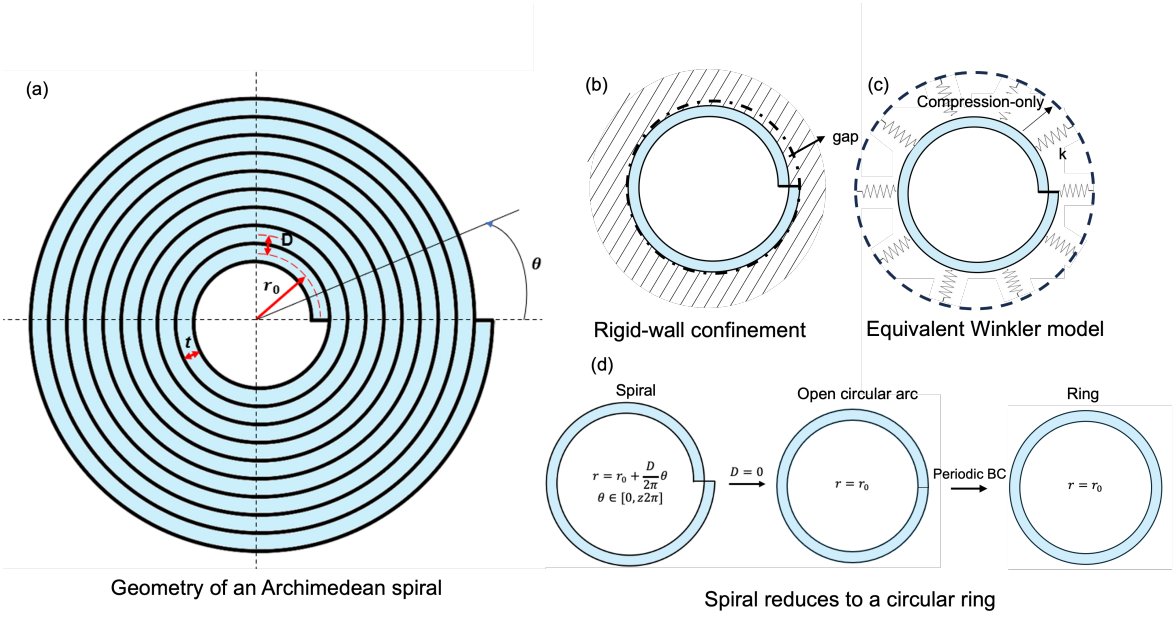

Figure 2: (a) Geometry of an Archimedean spiral. (b) and (c) Schematic illustration of the rigid confinement and its equivalent representation. (b) A one-turn Archimedean spiral confined by a rigid circular ring. Owing to the geometric mismatch between the spiral outer boundary and the circular confinement, a finite gap may exist locally. (c) An equivalent representation in which the rigid confinement is modeled by a distributed unilateral (compression-only) spring with stiffness k, which is activated only when the spiral contacts the rigid wall. (d) Schematic illustration of a one-turn Archimedean spiral strip with finite thickness. D denotes the radial increment per full turn of the spiral; in the limit $D \to 0$, the spiral degenerates into a circular ring.

to satisfy a plane-strain condition. For simplicity, the width of the spiral cylinder is normalized to $b = 1$.

Within this cross-sectional plane (Fig. 1, the spiral structure can be simplified to a one-dimensional mechanical problem, analogous to classical beam or ring buckling (Timoshenko and Goodier, 1970). Its mechanical behavior is described using beam theory with bending stiffness EI and extensional stiffness EA, where E is the elastic modulus, $A = bh$ is the cross-sectional area, and $I = bh^3/12$ is the second moment of area of the beam cross section. The spiral is subjected to a prescribed thermal or chemical eigenstrain, while contact with the surrounding rigid ring is enforced through a unilateral (no-penetration) constraint. Under these geometric and contact constraints, the imposed eigenstrain is largely converted into internal stresses within the spiral structure.

2.3. Arc-length coordinate system

The 1D problem is most convenient to be analyzed in the arc-length coordinate system. Specifically,for a given spiral with fixed r_0 and EI, the position of any point on the spiral can be specified by a single parameter, the arc length s. In the following analysis, we perform energy integration in the arc-length coordinate system, but express all quantities in terms of the angular parameter θ, treating θ as the parameter that defines the arc length $s(\theta)$. The arc length differential should satisfy the geometrical relation:

$$ds^2 = dr^2 + (rd\theta)^2. \tag{2}$$

Thereby, the Jacobian function between the body-fixed arc length coordinate and the polar coordinate can be defined as:

$$J(\theta) = \frac{ds}{d\theta} = \sqrt{r^2 + \left(\frac{dr}{d\theta}\right)^2}. \tag{3}$$

For an Archimedean spiral,

$$J(\theta) = \sqrt{r_0^2 + \frac{D}{\pi} r_0 \theta + \left(\frac{D}{2\pi}\right)^2 (1 + \theta^2)}. \tag{4}$$

2.4. Sources of internal loads

We consider structural instability induced by volumetric changes. In general, such changes give rise to an eigenstrain tensor $\boldsymbol{\varepsilon}^{\text{eigen}}$, which represents the stress-free deformation the material would undergo in the absence of mechanical constraints.

For diffusion-induced (chemical) swelling, as encountered in lithium-ion batteries (Shi et al., 2026), the eigenstrain tensor is

$$\boldsymbol{\varepsilon}^{\text{eigen}} = \boldsymbol{\beta}_{\text{eff}}\, \Delta c, \tag{5}$$

where $\boldsymbol{\beta}_{\text{eff}}$ is the effective chemical expansion coefficient tensor and Δc denotes the local change in species concentration. Similarly, when swelling is induced by a temperature rise, the eigenstrain tensor takes the form

$$\boldsymbol{\varepsilon}^{\text{eigen}} = \boldsymbol{\alpha}_{\text{eff}}\, \Delta T, \tag{6}$$

where $\boldsymbol{\alpha}_{\text{eff}}$ is the effective coefficient of thermal expansion tensor and ΔT denotes the local temperature change. Equations (5) and (6) share the same mathematical structure. Moreover, the governing transport laws—Fick's law for diffusion and Fourier's law for heat conduction—possess analogous linear forms. Consequently, these two physical fields are often treated interchangeably in computational modeling (Shi et al., 2026). In what follows, we adopt a unified eigenstrain description that encompasses both mechanisms.

When anisotropy is considered, $\boldsymbol{\beta}_{\text{eff}}$ and $\boldsymbol{\alpha}_{\text{eff}}$ are symmetric second-order tensors whose components may differ in the tangential, normal, and out-of-plane directions. In the isotropic limit, both tensors reduce to scalar multiples of the identity, $\boldsymbol{\alpha}_{\text{eff}} = \alpha_{\text{eff}}\, \mathbf{I}$, and the eigenstrain is purely dilatational.

For the beam model employed in this study, the eigenstrain tensor is projected onto the tangential direction of the spiral centerline. The tangential component,

$$\varepsilon_{tt}^{\text{eigen}}(\theta) = \boldsymbol{e}_t \cdot \boldsymbol{\varepsilon}^{\text{eigen}} \cdot \boldsymbol{e}_t, \tag{7}$$

governs the axial stretching of the beam and is therefore the component directly responsible for generating compressive resultants under confinement. The normal component $\varepsilon_{nn}^{\text{eigen}}$ produces a through-thickness expansion that alters the inter-layer gap in

multi-turn spirals but does not contribute to the tangential force resultant N. For a one-dimensional beam model, $\varepsilon_{nn}^{\text{eigen}}$ enters only through the contact conditions (Section 3.2.3) and is not required in the constitutive relation for N.

With this projection, the total tangential strain is decomposed additively into elastic and eigenstrain contributions,

$$\varepsilon_{tt} = \varepsilon_{tt}^{\text{elastic}} + \varepsilon_{tt}^{\text{eigen}}, \tag{8}$$

where ε_{tt} denotes the Green–Lagrange tangential strain derived in Section 3. The tangential force resultant is related to the elastic part alone,

$$N = EA\,\varepsilon_{tt}^{\text{elastic}} = EA\big(\varepsilon_{tt} - \varepsilon_{tt}^{\text{eigen}}\big), \tag{9}$$

with $N > 0$ denoting tension.

Two limiting cases illustrate the role of mechanical constraint. If the spiral is free to expand without any geometric restriction, the total strain accommodates the eigenstrain exactly, $\varepsilon_{tt} = \varepsilon_{tt}^{\text{eigen}}$, the elastic strain vanishes, $N = 0$, and no instability arises. In contrast, when the spiral is fully constrained so that tangential extension is suppressed ($\varepsilon_{tt} = 0$), the elastic strain equals the negative of the eigenstrain, $\varepsilon_{tt}^{\text{elastic}} = -\varepsilon_{tt}^{\text{eigen}}$, and the resulting compressive tangential force $N = -EA\,\varepsilon_{tt}^{\text{eigen}}$ may trigger buckling. For simplicity, intermediate cases with partial constraint are not considered in this study; we focus on the fully constrained limit and derive the corresponding critical buckling condition.

2.5. Confinement and constraint

Under eigenstrain loading, a spiral structure develops compressive tangential forces only if its free expansion is kinematically restricted. Two distinct sources of constraint are relevant to the present problem.

The first is *external confinement*. The exterior of the spiral is enclosed by a rigid circular ring (Fig. 2(b)), representative of the cylindrical casing that surrounds battery jelly rolls, sheet metal coils, and similar industrial components. The rigid wall prevents outward radial expansion, and the resulting contact generates compressive normal tractions that push back on the spiral. Because the wall cannot pull the spiral, contact is inherently unilateral: it resists penetration but permits separation. For an arbitrary

sing-turn ring in the spiral, we describe the ring–spiral interaction using a one-sided Winkler foundation. Normal contact pressure/traction produced by penalty model is $q_n = k\,H(w)\,w$ (Fig. 2(c)).

The second is *internal kinematic locking*. Because the spiral is an open-ended structure, external confinement alone does not fully suppress free expansion—the two ends can separate or slide, partially relieving the eigenstrain. In a single-turn spiral, this relief mechanism must be artificially suppressed (for instance, by coupling the displacements at the two ends) to produce the compressive resultants required for buckling. In multi-turn coils, however, adjacent layers press against one another under eigenstrain loading, and the resulting turn-to-turn contact tractions restrict both radial separation and tangential sliding. This inter-layer self-contact provides a natural kinematic locking that converts eigenstrain into compressive stress accumulation without the need for artificial end constraints.

To obtain a tractable theory while retaining the essential mechanics, we study two complementary configurations:

(i) A *one-turn Archimedean spiral confined by a rigid ring*, which isolates the eigenstrain-to-compression mechanism and the role of unilateral wall contact in a setting amenable to analytical treatment.

(ii) A *multi-turn spiral with turn-to-turn self-contact*, in which inter-layer interactions provide the kinematic locking that arises naturally in layered coils, eliminating the need for artificial end constraints.

The mathematical formulations of both the wall contact and the inter-layer contact are developed in the theoretical framework (Section 3).

2.6. Nondimensionalization and governing dimensionless groups

To reduce the parameter space and identify the controlling mechanics, we nondimensionalize the formulation using the initial (inner) radius r_0 as the reference length. This choice is natural because r_0 is prescribed for every configuration and remains fixed as the number of turns or layer thickness varies.

2.6.1. Dimensionless variables

We introduce the dimensionless field variables

$$\bar{u}(\theta) = \frac{u(\theta)}{r_0}, \qquad \bar{w}(\theta) = \frac{w(\theta)}{r_0}, \tag{10}$$

and the dimensionless geometric quantities

$$\bar{r}(\theta) = \frac{r(\theta)}{r_0}, \qquad \bar{s} = \frac{s}{r_0}, \qquad \bar{J}(\theta) = \frac{J(\theta)}{r_0}, \qquad \bar{\kappa}(\theta) = \kappa(\theta)\, r_0. \tag{11}$$

With these definitions, arc-length derivatives scale as $d/ds = (1/r_0)\, d/d\bar{s}$, while $d/d\theta$ is unchanged.

2.6.2. Dimensionless geometry

For an Archimedean spiral $r(\theta) = r_0 + b\theta$ with $b = D/(2\pi)$, we define the dimensionless pitch and radial increment

$$\hat{b} = \frac{b}{r_0}, \qquad \hat{D} = \frac{D}{r_0} = 2\pi\hat{b}. \tag{12}$$

The outer radius is $r_{\text{out}} = r_0 + DN_t$, so the dimensionless outer radius is

$$\hat{r}_{\text{out}} \equiv \frac{r_{\text{out}}}{r_0} = 1 + N_t\, \hat{D}. \tag{13}$$

Thus, once r_0 is chosen as the reference length, the spiral geometry is fully parameterized by $(N_t,\, \hat{D})$, with $\hat{r}_{\text{out}}$ following from Eq. (13).

In multi-turn coils where adjacent turns are in self-contact, the radial increment per turn equals the layer thickness ($D = t$), giving $\hat{D} = \hat{t}$ with $\hat{t} = t/r_0$. The dimensionless thickness $\hat{t}$ and the number of turns N_t then serve as the two independent geometric parameters.

2.6.3. Dimensionless mechanical quantities

Two key stiffness scales are the extensional stiffness EA and bending stiffness EI. Their ratio defines a dimensionless coupling parameter

$$\Gamma \equiv \frac{EI}{EA\, r_0^2}, \tag{14}$$

which measures the relative importance of bending over stretching at length scale r_0. For a rectangular cross-section with unit out-of-plane thickness ($A = h$, $I = h^3/12$), $\Gamma = \hat{h}^2/12$ where $\hat{h} = h/r_0$.

The eigenstrain amplitude is naturally dimensionless:

$$\varepsilon^{\text{eigen}}(\theta) = \alpha_{\text{eff}}\,\Delta T(\theta) \quad \text{or} \quad \varepsilon^{\text{eigen}}(\theta) = \beta_{\text{eff}}\,\Delta c(\theta). \tag{15}$$

Under full constraint, the induced compressive resultant scales as $N \sim -EA\,\varepsilon^{\text{eigen}}$. We define the dimensionless load

$$\bar{N} \equiv \frac{N\,r_0^2}{EI}, \tag{16}$$

which can equivalently be written as $\bar{N} = N/(EA\,\Gamma)$, connecting the dimensionless load to the strain-like measure $N/(EA)$.

The unilateral wall contact stiffness k is nondimensionalized as

$$\bar{k} \equiv \frac{k\,r_0^4}{EI}. \tag{17}$$

For the ring limit with $\hat{R} = R/r_0$, the contact term in the dimensionless governing equation carries the coefficient $\bar{k}\,\hat{R}^4$.

In the analytical development, contact is assumed frictionless. In the multi-turn computational study, Coulomb friction is introduced and characterized by the dimensionless coefficient μ.

2.6.4. Summary of governing dimensionless groups

Using r_0 as the reference length, the eigenstrain-driven confined spiral problem is governed by the following independent dimensionless parameters:

$$\underbrace{N_t,\ \hat{D}\ (\text{or equivalently } \hat{t})}_{\text{geometry}}, \qquad \underbrace{\Gamma}_{\text{stiffness ratio}}, \qquad \underbrace{\bar{k}}_{\text{confinement}}, \qquad \underbrace{\varepsilon^{\text{eigen}} \text{ or } \bar{N}}_{\text{load}}, \tag{18}$$

with μ added only in the multi-turn frictional parametric study. The analytical solutions (Section 4), computational results (Section 5), and parametric trends (Section 5.4) are all interpreted in terms of these groups.

3. Theoretical Framework

3.1. Kinematics

The deformed position vector of the structure can be described as

$$\boldsymbol{x}(s) = \boldsymbol{X}(s) + u(s)\,\boldsymbol{t}(s) + w(s)\,\boldsymbol{n}(s), \tag{19}$$

where $\boldsymbol{X}$ is the undeformed reference position, $\boldsymbol{x}$ is the deformed position, $\boldsymbol{t}$ is the tangential unit vector of the spiral (undeformed), $\boldsymbol{t} = d\boldsymbol{X}/ds$, $\boldsymbol{n}$ is the outward normal unit vector of the spiral(undeformed), u is the displacement along the tangential unit vector, and w is the displacement along outward normal.

Taking the first derivative of Eq. (19) in terms of s yields:

$$\boldsymbol{x}' = \underbrace{(1 + u' + \kappa w)}_{\lambda}\boldsymbol{t} + \underbrace{(w' - \kappa u)}_{\eta}\boldsymbol{n}, \tag{20}$$

where the operator $'$ denotes differentiation with respect to the arc-length parameter s, λ represents the tangential stretch (extension) of the centerline, and η represents the normal rotation of the centerline. Here, the Frenet–Serret formulas for differentiable curves (Mate, 2017) has been applied, i.e., $\boldsymbol{t}' = -\kappa\boldsymbol{n}, \boldsymbol{n}' = \kappa\boldsymbol{t}$, where κ is the original curvature of the spiral.

The Green-Lagrange tangential strain is thereby:

$$\varepsilon_{tt}(s) = \frac{1}{2}\left(\|x'\|^2 - 1\right) = (u' + \kappa w) + \frac{1}{2}\left[(u' + \kappa w)^2 + (w' - \kappa u)^2\right], \tag{21}$$

A simplified version can be obtained by retaining the leading geometric nonlinear contribution associated with the transverse displacement gradient and neglecting the remaining higher-order terms involving the tangential displacement and curvature-coupled components:

$$\varepsilon_{tt}(s) \approx (u' + \kappa w) + \frac{1}{2}(w')^2, \tag{22}$$

which is the total strain at an arbitrary point of a beam undergoing moderately large deflection (Wierzbicki and Ling, 2024).

For a planar curve described in polar coordinates as $r(\theta)$, the original undeformed curvature is given by

$$\kappa(\theta) = \frac{r^2 + 2(r_\theta)^2 - r\, r_{\theta\theta}}{\left(r^2 + (r_\theta)^2\right)^{3/2}}, \tag{23}$$

where the subscripts denote partial derivatives, e.g., $r_\theta = dr/d\theta$, $r_{\theta\theta} = d^2r/d\theta^2$.

For an Archimedean spiral $r = r_0 + b\theta \quad (b \equiv D/2\pi)$,

$$\kappa(\theta) = \frac{r^2 + 2b^2}{(r^2 + b^2)^{3/2}}. \tag{24}$$

The unit vector in the tangential direction of the deformed frame is

$$\tilde{\boldsymbol{t}} = \frac{\boldsymbol{x_s}}{|\boldsymbol{x_s}|} \approx \boldsymbol{t} + \eta\boldsymbol{n}, \tag{25}$$

which demonstrates the role of η as an effect of rotation.

Its derivative with respect to the deformed arc-length parameter $\tilde{s}$ is

$$\frac{d\tilde{\boldsymbol{t}}}{d\tilde{s}} = \frac{d\tilde{\boldsymbol{t}}}{ds}\frac{ds}{d\tilde{s}} \approx \frac{1}{\lambda}\frac{d\tilde{\boldsymbol{t}}}{ds} \approx (1 - u_s + \kappa w)\left[(\kappa + \eta_s)\boldsymbol{n} - \kappa\eta\,\boldsymbol{t}\right], \tag{26}$$

and the deformed curvature is obtained:

$$\tilde{\kappa} \approx \frac{d\tilde{\boldsymbol{t}}}{d\tilde{s}} \cdot \boldsymbol{n} \approx (1 - u_s + \kappa w)(\kappa + \eta_s). \tag{27}$$

The change in curvature is calculated:

$$\Delta\kappa = \tilde{\kappa} - \kappa \approx \eta_s - \kappa u_s + \kappa^2 w = w_{ss} + \kappa_s u + \kappa^2 w. \tag{28}$$

A limit example: For a circular ring, the curvature is constant, $\kappa = 1/R$, leading to $\kappa_s = 0$. The arc-length parameter is related to the angular coordinate by $s = R\theta$. As a result, the change in curvature is expressed as

$$\Delta\kappa_{\text{ring}} = w_{ss} + \kappa^2 w = \frac{1}{R^2} w_{\theta\theta} + \frac{1}{R^2} w = \frac{1}{R^2}(w_{\theta\theta} + w), \tag{29}$$

which agrees with classical theories (Wierzbicki and Ling, 2024).

3.2. Constitutive relations

Assuming linear elastic behaviour throughout, the tangential force resultant and bending moment are related to the kinematic measures derived in Section 3.1 by

$$N = EA\,\varepsilon_{tt}^{\text{elastic}}, \qquad M = EI\,\Delta\kappa, \tag{30}$$

where $\varepsilon_{tt}^{\text{elastic}} = \varepsilon_{tt} - \varepsilon_{tt}^{\text{eigen}}$ is the elastic part of the tangential strain (Eq. 8), κ is the reference curvature of the undeformed spiral, and $\tilde{\kappa}$ is the deformed curvature. By convention, $N > 0$ denotes tension and a positive $\Delta\kappa$ corresponds to an increase in curvature (inward tightening for the spiral geometry).

3.3. Energy analysis

The total potential energy of the confined spiral consists of three contributions:

$$U_{\text{total}} = U_{\text{stretching}} + U_{\text{bending}} + \Pi_{\text{contact}}. \tag{31}$$

The stretching and bending energies store the elastic strain energy arising from tangential deformation and curvature change of the centerline, respectively; the contact potential accounts for the unilateral interaction with the rigid wall and, in the multi-turn case, the turn-to-turn inter-layer contact. We develop each term below, assuming linear elastic constitutive behaviour throughout.

3.3.1. Stretching energy

The stretching energy stored in the spiral is the elastic energy associated with tangential (membrane) deformation of the centerline. Using the constitutive relation (30) and the arc-length–to–θ mapping $ds = J\,d\theta$, the stretching energy integrated along the spiral is

$$U_{\text{stretching}} = \frac{1}{2}\int_{\gamma} \frac{N^2}{EA}\,ds = \frac{EA}{2}\int_0^{2\pi N_t} \left(\varepsilon_{tt}^{\text{elastic}}(\theta)\right)^2 J(\theta)\,d\theta, \tag{32}$$

where the elastic strain $\varepsilon_{tt}^{\text{elastic}} = \varepsilon_{tt} - \varepsilon_{tt}^{\text{eigen}}$ follows from the strain decomposition (8), and the total tangential strain $\varepsilon_{tt}(\theta)$ is given by the kinematic relation (22) derived in Section 3.1.

3.3.2. Bending energy

The bending energy arises from changes in curvature of the centerline relative to the undeformed configuration. Using the constitutive relation (30),

$$U_{\text{bending}} = \frac{1}{2}\int_{\gamma} \frac{M^2}{EI}\,ds = \frac{EI}{2}\int_0^{2\pi N_t} (\Delta\kappa)^2\, J(\theta)\,d\theta, \tag{33}$$

where the curvature change $\Delta\kappa = \tilde{\kappa} - \kappa$ is expressed in the θ-parametrization by Eq. (28).

3.3.3. Contact potential energy

As described in Section 2.5, two types of contact interaction arise in the confined spiral: (i) contact between the outermost layer and the surrounding outside ring, and (ii) turn-to-turn contact between adjacent inner layers. Both interactions are unilateral (compression-only) and are modeled here as one-sided penalty foundations using the Heaviside step function

$$H(x) = \begin{cases} 0, & x < 0, \\ 1, & x \geq 0, \end{cases} \tag{34}$$

as the activation switch.

Wall contact. The outermost layer, $\theta \in [2\pi(N_t - 1),\, 2\pi N_t]$, is confined by the rigid ring (Fig. 2(b)). Because the spiral outer boundary is not perfectly circular, a small geometric mismatch exists between the spiral and the confinement; however, this gap is negligible when the layer thickness is much smaller than the confinement radius, and the outermost layer is treated as initially in contact with the wall.

Following the Winkler foundation approach (Bhattacharya et al., 2021), the rigid wall is replaced by a distributed, one-sided spring foundation (Fig. 2(c)) that resists outward penetration but permits inward separation. The wall contact potential energy is

$$\Pi_{\text{wall}} = \frac{1}{2}\int_{2\pi(N_t-1)}^{2\pi N_t} k_w\, H\big(w(\theta)\big)\, w(\theta)^2\, J(\theta)\, d\theta, \tag{35}$$

where k_w is the wall penalty stiffness and $w(\theta)$ is the outward-normal displacement of the centerline ($w > 0$ toward the wall). The Heaviside function activates the penalty only when the spiral pushes into the wall ($w \geq 0$); when the spiral separates ($w < 0$), the foundation transmits no traction.

Turn-to-turn contact. Within the inner windings, $\theta \in [0,\, 2\pi(N_t - 1)]$, adjacent layers may come into contact under eigenstrain loading. The radial gap between a layer at angle θ and its outer neighbor is

$$g(\theta) = g_0 + \big[w(\theta + 2\pi) - w(\theta)\big], \tag{36}$$

where g_0 is the initial clearance. Positive g indicates separation; negative g indicates overclosure (penetration). The inter-layer contact potential energy is

$$\Pi_{\text{layer}} = \frac{1}{2}\int_{0}^{2\pi(N_t-1)} k_N\, H\big(-g(\theta)\big)\, g(\theta)^2\, J(\theta)\, d\theta, \tag{37}$$

where k_N is the inter-layer normal penalty stiffness and $H(-g)$ activates the penalty only under overclosure ($g < 0$).

Total contact energy. The total contact contribution to the potential energy is the sum of the wall and inter-layer terms:

$$\Pi_{\text{contact}} = \Pi_{\text{layer}} + \Pi_{\text{wall}}. \tag{38}$$

One-turn reduction. For the prototype one-turn spiral ($N_t = 1$, $\theta \in [0, 2\pi]$) confined by a outside ring, no inner windings exist and $\Pi_{\text{layer}} = 0$. The contact energy reduces to

$$\Pi_{\text{contact}} = \frac{1}{2}\int_{0}^{2\pi} k\, H\big(w(\theta)\big)\, w(\theta)^2\, J(\theta)\, d\theta, \tag{39}$$

where k denotes the wall penalty stiffness for the one-turn configuration. This reduced form is used in the variational derivation and the Rayleigh–Ritz estimate that follow.

3.4. Variational formulation and governing equations

3.4.1. Stationarity of the total potential energy

Equilibrium configurations of the confined spiral correspond to stationary points of the total potential energy $U_{\text{total}} = U_{\text{stretching}} + U_{\text{bending}} + \Pi_{\text{contact}}$. The governing equations and associated natural boundary conditions are obtained by requiring the first variation to vanish for all admissible variations δu and δw:

$$\delta U_{\text{total}} = \delta U_{\text{stretching}} + \delta U_{\text{bending}} + \delta \Pi_{\text{contact}} = 0. \tag{40}$$

Taking the variation of each energy term (Eqs. 32, 33, and 39), integrating by parts in θ, and collecting the coefficients of δu and δw separately (see Appendix Appendix A for details) yields the following Euler–Lagrange equations.

Tangential equilibrium (coefficient of δu).

$$-EA\left(\varepsilon_{tt}^{\text{elastic}}\right)_{,\theta} + EI\,(\Delta\kappa)\,\kappa_{,\theta} = 0. \tag{41}$$

Normal equilibrium (coefficient of δw).

$$-EA\left(\varepsilon_{tt}^{\text{elastic}}\,\kappa\,J + \frac{d}{d\theta}\left(\varepsilon_{tt}^{\text{elastic}}\,\frac{1}{J}\,w_{,\theta}\right)\right) + EI\left(J\,(\Delta\kappa)\,\kappa^2 + \frac{d}{d\theta}\left(\frac{1}{J}\,(\Delta\kappa)_{,\theta}\right)\right) + k\,H(w)\,w\,J = 0. \tag{42}$$

The first group of terms in each equation originates from the stretching energy and couples the tangential force to membrane deformation; the second group originates from the bending energy and involves the curvature change; the contact term appears only in the normal equation and acts as a one-sided restoring force proportional to the outward displacement. Together, these two equations govern the coupled tangential–normal response of the spiral centerline under eigenstrain loading with unilateral confinement.

3.4.2. Governing equations in resultant form

Introducing the tangential force resultant $N = EA\,\varepsilon_{tt}^{\text{elastic}}$ and the bending moment $M = EI(\tilde{\kappa} - \kappa)$ from Eq. (30), Eqs. (41)–(42) can be rewritten as the following spiral-path Föppl–von Kármán-type system.

Tangential equilibrium.

$$N_{,\theta} = M\,\kappa_{,\theta}. \tag{43}$$

Normal equilibrium.

$$-\left(N\,\kappa\,J+\frac{d}{d\theta}\left(\frac{N}{J}\,w_{,\theta}\right)\right)+\left(J\,M\,\kappa^2+\frac{d}{d\theta}\left(\frac{1}{J}\,M_{,\theta}\right)\right)+k\,H(w)\,w\,J=0. \tag{44}$$

In Eq. (43), the tangential force varies along the spiral only where the curvature is non-uniform ($\kappa_{,\theta}\neq 0$); for a circular ring ($\kappa_{,\theta}=0$), the tangential force is constant, recovering the classical result. In Eq. (44), the first group represents the destabilizing effect of the compressive resultant acting through the curved geometry, the second group is the bending resistance, and the last term is the one-sided contact restoring force.

Boundary conditions. At the two ends of the spiral ($\theta=0$ and $\theta=2\pi N_t$), either the kinematic (essential) variable or the corresponding static (natural) resultant is prescribed:

$$\begin{cases} u=\bar{u} & \text{or} \quad N=\bar{N}, \\ w=\bar{w} & \text{or} \quad Q=\bar{Q}, \\ \dfrac{1}{J}\,w_{,\theta}=\bar{\psi} & \text{or} \quad M=\bar{M}, \end{cases} \tag{45}$$

where the effective shear force in the θ-parametrization is

$$Q=\frac{1}{J}\big(M_{,\theta}-N\,w_{,\theta}\big). \tag{46}$$

Straight-beam limit. As a consistency check, setting $\kappa=0$ and $J=1$ (initially straight beam with Cartesian coordinate x) reduces Eqs. (43)–(44) to the classical Föppl–von Kármán beam on a one-sided elastic foundation:

$$N_{,x}=0, \qquad -\big(N\,w_{,x}\big)_{,x}+\big(EI\,w_{,xx}\big)_{,xx}+k\,H(w)\,w=0, \tag{47}$$

confirming that the spiral-path formulation contains the standard beam–column model as a special case.

3.5. Dimensionless governing equations

Substituting the dimensionless variables defined in Section 2.6 into the governing equations (43)–(44) yields the dimensionless spiral-path Föppl–von Kármán system.

Tangential equilibrium.

$$\bar{N}_{,\theta} = \bar{M}\,\bar{\kappa}_{,\theta}, \tag{48}$$

where $\bar{M} = M\,r_0/(EI) = \bar{\bar{\kappa}} - \bar{\kappa}$ is the dimensionless bending moment.

Normal equilibrium.

$$-\left(\bar{N}\,\bar{\kappa}\,\bar{J} + \frac{d}{d\theta}\left(\frac{\bar{N}}{\bar{J}}\,\bar{w}_{,\theta}\right)\right) + \left(\bar{J}\,\bar{M}\,\bar{\kappa}^2 + \frac{d}{d\theta}\left(\frac{1}{\bar{J}}\,\bar{M}_{,\theta}\right)\right) + \bar{k}\,\bar{J}\,H(\bar{w})\,\bar{w} = 0. \tag{49}$$

Ring limit. In the zero-pitch limit ($\hat{D} \to 0$), the spiral degenerates into a circular ring of dimensionless radius $\hat{R} = R/r_0$, with constant Jacobian $\bar{J} = \hat{R}$, curvature $\bar{\kappa} = 1/\hat{R}$, and $\bar{\kappa}_{,\theta} = 0$. Equation (48) then gives $\bar{N} = \text{const}$, and Eq. (49) reduces to the dimensionless ring equation

$$-\left(\bar{N}\,\hat{R}^2\right)\bar{w}_{,\theta\theta} + \left(\bar{w}_{,\theta\theta\theta\theta} + 2\bar{w}_{,\theta\theta} + \bar{w}\right) + \left(\bar{k}\,\hat{R}^4\right)H(\bar{w})\,\bar{w} = 0, \tag{50}$$

where the base-state equilibrium has been subtracted as described in Appendix Appendix B. The ring equation is controlled by two dimensionless groups: $\bar{N}\hat{R}^2$, which measures the compressive resultant relative to bending stiffness, and $\bar{k}\hat{R}^4$, which measures the confinement stiffness relative to bending stiffness.

Equations (48)–(49) and their ring specialization (50) constitute the complete dimensionless problem statement.

4. Analytical Solutions

The dimensionless governing equations (48)–(49) define a nonlinear boundary-value problem with an unknown contact set, for which no general closed-form solution is available. In this section we develop analytical estimates for the critical compressive resultant through three complementary steps. First, we formulate a Rayleigh–Ritz energy approach that converts the stability problem into a one-parameter optimization over the detached arc length (Sections 4.1 and 4.2). Second, we specialize the spiral to the zero-pitch (circular ring) limit, which admits mode-dependent critical loads in closed form and serves as an analytical benchmark (Sections 4.3 and 4.4). Third, we collect all results in dimensionless form and compare the eigenstrain-loaded ring with the classical pressure-loaded ring (Section 4.5).

4.1. Rayleigh–Ritz estimate of the critical compressive resultant

To estimate the critical compressive resultant without solving the full free-boundary contact problem, we employ a Rayleigh–Ritz energy approach (Timoshenko and Gere, 2012).

4.1.1. Second-order energy and the Rayleigh quotient

We consider the onset of buckling as a bifurcation from a uniformly compressed pre-buckling state in which the spiral carries a constant tangential resultant N (compressive, $N < 0$) and the centerline remains undeflected. The stability of this state is governed by the sign of the second-order potential energy evaluated for small perturbations δu, δw about the base configuration.

The second-order stretching energy consists of two parts: the work done by the pre-buckling resultant through the second-order shortening associated with transverse deflection, and the membrane energy from any residual midplane stretching:

$$U^{(2)}_{\text{stretching}} = -\frac{1}{2}\,N \int_0^{2\pi} \frac{w_{,\theta}^2}{J}\,d\theta \;+\; \frac{1}{2}\,EA \int_0^{2\pi} \Big(\frac{u_{,\theta}}{J} + \kappa\, w\Big)^2 J\,d\theta. \tag{51}$$

The first term is destabilizing (it releases energy as the beam deflects); the second penalizes any tangential strain that accompanies the buckling mode.

The second-order bending energy is

$$U^{(2)}_{\text{bending}} = \frac{1}{2}\,EI \int_0^{2\pi} (\Delta\kappa)^2\, J\,d\theta, \tag{52}$$

and the contact energy for the one-turn spiral (Eq. 39) is

$$\Pi^{(2)}_{\text{contact}} = \frac{1}{2} \int_0^{2\pi} k\, H(w)\, w^2\, J\,d\theta. \tag{53}$$

At the critical load, the total second-order energy transitions from positive-definite to zero for the critical mode. Setting $U^{(2)}_{\text{stretching}} + U^{(2)}_{\text{bending}} + \Pi^{(2)}_{\text{contact}} = 0$ and solving for N yields the Rayleigh quotient

$$N_{\text{cr}} = \frac{EA \displaystyle\int_0^{2\pi} \Big(\frac{u_{,\theta}}{J} + \kappa w\Big)^2 J\,d\theta + EI \int_0^{2\pi} (\Delta\kappa)^2\, J\,d\theta + \int_0^{2\pi} k\, H(w)\, w^2\, J\,d\theta}{\displaystyle\int_0^{2\pi} \frac{w_{,\theta}^2}{J}\,d\theta}. \tag{54}$$

If the wall is assumed to be rigid, no deformation energy is stored in the wall. Moreover, if the contact is modeled as an ideal frictionless unilateral constraint, the contact force

does no virtual work for admissible perturbations. The second-order contact potential energy term, $\Pi^{(2)}_{\text{contact}}$, can be taken as zero. The effect of contact is therefore imposed through the admissible displacement constraints rather than through an explicit contact energy term. Therefore, we set $\Pi^{(2)}_{\text{contact}}$ term equal to 0.

$$N_{\text{cr}} = \frac{EI \int_0^{2\pi} (\Delta\kappa)^2 \, J \, d\theta + EA \int_0^{2\pi} \left(\frac{u_{,\theta}}{J} + \kappa w \right)^2 J \, d\theta}{\int_0^{2\pi} \frac{w_{,\theta}^2}{J} \, d\theta}, \tag{55}$$

which provides an upper bound on $|N_{\text{cr}}|$ for a kinematically admissible trial displacement (u, w).

4.1.2. Inextensibility approximation

For a slender spiral ($h \ll r_0$), the bending stiffness is much smaller than the extensional stiffness ($EI/(EA\, r_0^2) \ll 1$), and the spiral is well approximated as inextensible prior to buckling. We therefore enforce the linearized near inextensibility constraint

$$\frac{1}{J} \, u_{,\theta} + \kappa \, w \approx 0, \tag{56}$$

which eliminates the membrane energy term in Eq. (51) and reduces the Rayleigh quotient to

$$N_{\text{cr}} = \frac{EI \int_0^{2\pi} (\Delta\kappa)^2 \, J \, d\theta}{\int_0^{2\pi} \frac{w_{,\theta}^2}{J} \, d\theta}. \tag{57}$$

Here, Eq. (56) is a local description of inextensibility that strictly applies everywehre, while a global description that integrates over 0 to 2π is more acculate. We will discuss it in Section 6.5.

The constraint (56) also provides the kinematic link between u and w: given a trial deflection $w(\theta)$, the tangential displacement is obtained by integration,

$$u(\theta) \approx - \int_0^{\theta} \kappa(\eta) \, J(\eta) \, w(\eta) \, d\eta + C, \tag{58}$$

where C is a constant determined by the boundary conditions. This relation ensures that u enters the curvature change expression (Eq. 28) consistently with the inextensibility assumption. To satisfy the boundary conditions for the closed-end one-turn

spiral, $u(0) = u(2\pi), w(0) = w(2\pi)$, we have

$$\int_0^{2\pi} \kappa(\eta) J(\eta) w(\eta) d\eta \approx 0, \tag{59}$$

with

$$C = u(0) = u(2\pi). \tag{60}$$

Ring-limit check. For a circular ring ($\kappa = 1/R$, $J = R$), Eq. (56) gives $u_{,\theta} = -w$, the classical inextensional ring relation, confirming the correct sign and form.

4.1.3. Semi-analytical Rayleigh–Ritz estimate of inward buckling

A semi-analytical Rayleigh–Ritz framework was developed to estimate the critical compressive force of the confined Archimedean spiral and to interpret the corresponding inward instability mode. The spiral centerline was described by

$$r(\theta) = r_0 + b\theta, \tag{61}$$

where $b = p/(2\pi)$ and p is the spiral pitch. The arc-length Jacobian is therefore

$$J(\theta) = \sqrt{r^2 + b^2}, \tag{62}$$

such that

$$ds = J(\theta) d\theta. \tag{63}$$

The perturbation of the spiral is described by a tangential displacement $u(\theta)$ and a normal displacement $w(\theta)$. The sign convention is chosen such that $w > 0$ denotes outward motion, whereas $w < 0$ denotes inward motion. Since the rigid outer ring confines the inner spiral structure and restricts outward deformation, the admissible normal displacement is assumed to satisfy the unilateral constraint

$$w(\theta) \leq 0. \tag{64}$$

To be consistent with this constraint and to capture the localized deformation near the tied region, a Gaussian-like inward mode shape with a kink at $\theta = 0$ is introduced:

$$w(\theta) = -A_0 \exp\left(-\frac{\xi^2}{2\sigma^2}\right) \exp\left(-\beta|\xi|\right) \cos^2\left(\frac{\pi\xi}{2\phi}\right), \qquad |\xi| \leq \phi, \tag{65}$$

and

$$w(\theta) = 0, \qquad |\xi| > \phi. \tag{66}$$

Here,

$$\xi = \mathrm{wrap}(\theta - \theta_0) \tag{67}$$

denotes the wrapped angular distance from the center of the localized inward deformation. The negative sign indicates that the perturbation is directed inward, and A_0 controls the maximum perturbation amplitude. The Gaussian term determines the overall decay of the perturbation away from the center, with σ controlling its width. The factor $\exp(-\beta|\xi|)$ provides an additional kink-like localization near the deformation center, while the $\cos^2(\pi\xi/2\phi)$ term acts as a smooth cutoff so that the perturbation vanishes at $|\xi| = \phi$. Therefore, the perturbation is confined to a finite angular region $|\xi| \leq \phi$ and smoothly approaches zero at the boundary. The amplitude A_0 cancels in the Rayleigh quotient and therefore does not affect the predicted critical force.

The corresponding tangential displacement is first constructed from the local inextensibility relation of a curved beam. The axial stretching measure is written as

$$S = \frac{u_{,\theta}}{J} + \kappa w, \tag{68}$$

where κ is the curvature of the Archimedean spiral,

$$\kappa = \frac{r^2 + 2b^2}{(r^2 + b^2)^{3/2}}. \tag{69}$$

For a strictly inextensible perturbation, one would require

$$S = 0. \tag{70}$$

This gives

$$u_{,\theta} = -J\kappa w. \tag{71}$$

The tangential displacement $u(\theta)$ is then obtained by numerical integration of Eq. (71) along the spiral.

However, for the one-sided inward mode $w(\theta) \leq 0$, the displacement obtained from the local inextensibility condition generally does not satisfy the periodic or tied compatibility condition

$$u(0) = u(2\pi). \tag{72}$$

This incompatibility occurs because the inward-only mode tends to produce a nonzero net tangential drift when Eq. (71) is integrated over one period. Therefore, a linear

drift correction is applied to enforce Eq. (72). If the integrated tangential displacement has a net drift

$$\Delta u = u(2\pi) - u(0), \tag{73}$$

the corrected tangential displacement is defined as

$$u_{\mathrm{corr}}(\theta) = u(\theta) - \frac{\Delta u}{2\pi}\theta. \tag{74}$$

Correspondingly,

$$u_{\theta,\mathrm{corr}} = u_{,\theta} - \frac{\Delta u}{2\pi}. \tag{75}$$

After this correction, the stretching measure becomes

$$S = \frac{u_{\theta,\mathrm{corr}}}{J} + \kappa w. \tag{76}$$

Although the drift correction enforces the tied compatibility condition, it introduces a residual stretching strain. Therefore, the admissible inward perturbation is not strictly inextensible. Instead, it is interpreted as a constrained bending–stretching mode caused by the incompatibility between the unilateral inward constraint $w(\theta) \leq 0$ and the periodic compatibility condition on $u(\theta)$.

The critical compressive force is estimated using the Rayleigh quotient

$$N_{cr} = \frac{EI \int Q^2 J \, d\theta + EA \int S^2 J \, d\theta}{\int w_{,\theta}^2 / J \, d\theta}. \tag{77}$$

Here, the first term in the numerator represents the bending contribution, while the second term represents the stretching contribution. The curvature-change measure Q is expressed as

$$Q = A_1 w_{,\theta\theta} + A_2 w_{,\theta} + A_3 u + A_4 w, \tag{78}$$

where the geometry-dependent coefficients are

$$A_1 = \frac{1}{r^2 + b^2}, \tag{79}$$

$$A_2 = -\frac{br}{\left(r^2 + b^2\right)^2}, \tag{80}$$

$$A_3 = -\frac{br\left(r^2 + 4b^2\right)}{\left(r^2 + b^2\right)^3}, \tag{81}$$

and

$$A_4 = \frac{\left(r^2 + 2b^2\right)^2}{\left(r^2 + b^2\right)^3}. \tag{82}$$

Hence, the inward buckling problem can be solved semi-analytically by varying the two parameters ϕ and σ in the inward mode shape (Eq.65) to minimize the critical force N_{cr} over the admissible trial space:

$$N_{cr} = \min_{\phi,\sigma} \left[\frac{EI \int Q^2 J \, d\theta + EA \int S^2 J \, d\theta}{\int w_{,\theta}^2 / J \, d\theta} \right]. \tag{83}$$

This solution differs from traditional analytical solutions of buckling because the integral terms require computational codes for calculation. This semi-analytical estimate of the first inward instability mode also allows us to quantify the relative importance of bending and stretching energies, through the ratio

$$\frac{U_s}{U_b} = \frac{EA \int S^2 J \, d\theta}{EI \int Q^2 J \, d\theta}, \tag{84}$$

which evaluates whether the mode is bending-dominated or stretching-coupled. The contribution of contact will be elaborated on in the following section.

4.2. Glock decomposition: prescribed detached region

The Heaviside function in Eq. (57) couples the contact state to the unknown buckling mode, precluding a closed-form evaluation. We resolve this by adopting the approach introduced by Glock (Glock, 1977; Omara et al., 1997) for the buckling of confined liners: the circumference is decomposed into a *detached segment* $\theta \in [-\phi, \phi]$, where the spiral separates from the wall and deforms inward ($w \leq 0$), and a *contact segment* $\theta \in [\phi,\, 2\pi - \phi]$, where the spiral remains pressed against the rigid ring and $w = 0$.

Because $w = 0$ in the contact segment, all energy contributions are confined to the detached arc. The contact energy term vanishes (the spiral is separated from the wall where it deflects, and stationary where it contacts), and the Rayleigh quotient under inextensibility assumption (Eq.57) reduces to

$$N_{\mathrm{cr}}(\phi) = \frac{EI \displaystyle\int_{-\phi}^{\phi} (\Delta\kappa)^2 \, J \, d\theta}{\displaystyle\int_{-\phi}^{\phi} \frac{w_{,\theta}^2}{J} \, d\theta}. \tag{85}$$

The detached half-angle ϕ has already been treated as a parameter of the shape function for optimization, and the physically realized configuration corresponds to the value that minimizes $|N_{\mathrm{cr}}(\phi)|$, representing the most energetically favorable detachment geometry.

4.3. Special case: reduction to a circular ring

To isolate the instability mechanism and provide an analytical benchmark, we consider the zero-pitch limit of the Archimedean spiral (Fig. 2(d)). As the pitch vanishes, i.e., $D \to 0$, the centerline radius becomes independent of the angular coordinate,

$$r(\theta) = r_0 + \frac{D}{2\pi}\theta \;\longrightarrow\; R,$$

and the Archimedean spiral degenerates into a circular centerline with constant Jacobian $J = R$ and curvature $\kappa = 1/R$, with $\kappa_{,\theta} = 0$. However, this geometric limit alone produces an open circular arc parameterized over $\theta \in [0, 2\pi]$. To recover a closed circular ring, the two ends of the arc must be identified by imposing periodic boundary conditions, such that the displacement and rotation fields, together with the corresponding force and moment resultants, are continuous across $\theta = 0$ and $\theta = 2\pi$. Therefore, the circular ring can be regarded as the zero-pitch, periodically closed limit of the Archimedean spiral.

4.3.1. Ring governing equation

Substituting $J = R$ and $\kappa = 1/R$ into the dimensional governing equations (43)–(44) yields the ring equilibrium equation (see Appendix Appendix B for the detailed reduction):

$$-\frac{N}{R}\, w_{,\theta\theta} + \frac{EI}{R^3}\big(w_{,\theta\theta\theta\theta} + 2w_{,\theta\theta} + w\big) + k\, R\, H(w)\, w = 0, \tag{86}$$

where N is the constant circumferential compressive resultant (positive in tension) and the base-state equilibrium has been subtracted as described in Appendix Appendix B. The tangential equilibrium (43) reduces to $N_{,\theta} = 0$, confirming that the hoop force is uniform around the ring.

4.3.2. Mode-dependent critical load

Assuming a Fourier trial mode $w(\theta) = A\cos(n\theta)$ with $n \geq 2$ (the $n = 1$ mode is a rigid-body translation), substitution into Eq. (86) yields the critical compressive resultant for each admissible mode:

$$N_{\mathrm{cr}}(n) = -\frac{EI}{R^2}\,\frac{(n^2-1)^2}{n^2} - \frac{kR^2}{n^2}\,H(w), \qquad n = 2, 3, 4, \ldots \tag{87}$$

The first term is the bending resistance and the second is the contact stiffness contribution. Because the penalty regularization permits small overclosure, Eq. (87) is used

as an analytical baseline to capture scaling and mode dependence; exact unilateral contact corresponds to a complementarity problem with an unknown active set, which is discussed in Section 6.

4.3.3. Pre-buckling contact state: limiting baselines

Depending on the pre-buckling contact condition, two limiting cases provide analytical bounds.

If the ring is fully detached ($H \equiv 0$), the contact stiffness vanishes:

$$N_{\mathrm{cr}}^{\mathrm{det}}(n) = -\frac{EI}{R^2}\frac{(n^2-1)^2}{n^2}, \qquad n \geq 2. \tag{88}$$

If the ring is fully confined and contact is active along the entire circumference ($H \equiv 1$):

$$N_{\mathrm{cr}}^{\mathrm{full}}(n) = -\frac{EI}{R^2}\frac{(n^2-1)^2}{n^2} - \frac{kR^2}{n^2}, \qquad n \geq 2. \tag{89}$$

Equations (88) and (89) bracket the true critical load: the detached limit provides a lower bound on $|N_{\mathrm{cr}}|$ and the fully contacting limit provides an upper bound. Here, k is the wall penalty stiffness, which depends on the material properties of the outer wall.

4.4. Semi-analytical Rayleigh–Ritz estimate for a ring

The Fourier-mode analysis of Section 4.3.2 assumes a global sinusoidal mode over the entire circumference. However, if the outer wall is rigid, this global sinusoidal assumption may no longer be valid because the deformation is geometrically constrained by the wall. In particular, partial wall contact can localize the deformation and restrict the admissible displacement field. To address this limitation and to account for the effect of partial wall contact, we apply the Glock decomposition. (Section 4.2) to the ring, which yields a closed-form expression for $N_{\mathrm{cr}}(\phi)$.

For a ring ($J = R$, $\kappa = 1/R$, $\kappa_{,\theta} = 0$), the curvature change reduces to $\tilde{\kappa} - \kappa = (w_{,\theta\theta} + w)/R^2$ (Eq. 29), and the inextensibility relation gives $u_{,\theta} = -w$. The Rayleigh quotient (85) becomes

$$N_{\mathrm{cr}}(\phi) = \frac{EI}{R^2}\frac{\displaystyle\int_{-\phi}^{\phi}(w_{,\theta\theta}+w)^2\,d\theta}{\displaystyle\int_{-\phi}^{\phi}w_{,\theta}^2\,d\theta}. \tag{90}$$

To satisfy the inextensibility condition, eq.59 can be reduce to

$$\int_0^{2\pi} w(\theta)d(\theta) = 0, \tag{91}$$

as $w = 0$ outside the interval $[-\phi, \phi]$. We can further obtain,

$$\int_{-\phi}^{\phi} w(\theta)d(\theta) = 0, \tag{92}$$

The trial function should satisfies both displacement and slope continuity at the take-off points: $w(\pm\phi) = 0$ and $w_{,\theta}(\pm\phi) = 0$, as well as the inextensibility condition. These conditions ensure smooth detachment from the rigid wall, consistent with the Glock model (Glock, 1977; Omara et al., 1997).

The pre-buckling compressive force is generated by constraining the swelling-induced eigenstrain of the spiral layer. Under strong tangential constraint, the free expansion is largely suppressed, leading to a compressive membrane force $N = EA\varepsilon$. However, during local inward buckling, enforcing strict inextensibility on the perturbation field would impose a global compatibility condition that excludes single-sided deformation modes. Therefore, the buckling formulation retains the stretching energy and treats the centerline as nearly, but not exactly, inextensible. This treatment is also consistent with the discussion in the spiral section above. Unlike classical sinusoidal ring modes, which contain both inward and outward radial displacements, the prescribed Gaussian-like mode enforces a one-sided inward deformation and localizes the instability near the imposed imperfection. This choice is therefore more consistent with the observed collapse mechanism, where buckling initiates from a localized defect and subsequently evolves into an inward deformation pattern.

Therefore, we choose the following admissible localized Gaussian trial function:

$$w(\theta) = -A_0 \exp\left(-\frac{\theta^2}{2\sigma^2}\right) \exp\left(-\beta\sqrt{\theta^2 + \varepsilon^2}\right) \cos^2\left(\frac{\pi\theta}{2\phi}\right). \tag{93}$$

The trial function describes a localized inward deformation centered at $\theta = 0$. The negative sign ensures that the normal displacement is directed inward, so that $w(\theta) \leq 0$ within the prescribed deformation region. The parameter A_0 controls the maximum deformation amplitude. The Gaussian term $\exp(-\theta^2/2\sigma^2)$ localizes the deformation near the center, with σ controlling the width of the localized region. The additional exponential factor $\exp(-\beta\sqrt{\theta^2 + \epsilon^2})$ further modulates the decay of the deformation away

from the center, where β controls the decay rate and ϵ is introduced as a small regularization parameter to avoid non-smooth behavior at $\theta = 0$. The factor $\cos^2(\pi\theta/2\phi)$ acts as a smooth cutoff function, forcing the deformation to vanish at the boundary $\theta = \pm\phi$. Therefore, this function represents a smooth, localized, inward perturbation with finite angular extent.

After defining the admissible trial function, the semi-analytical critical load is obtained through an energy minimization procedure. The trial mode shape $w(\theta)$ is substituted into the total potential energy, including the bending energy, stretching energy, and the work done by the compressive load. This gives the total potential energy as a function of the unknown mode amplitude A_0 and the applied load N:

$$\Pi(A_0, N) = U_{\text{bending}} + U_{\text{stretching}} - W_N. \tag{94}$$

The critical load corresponds to the point at which the undeformed equilibrium state loses stability. Therefore, the second variation of the total potential energy with respect to the perturbation amplitude is set to zero:

$$\frac{\partial^2 \Pi}{\partial A_0^2} = 0. \tag{95}$$

Solving this condition gives the semi-analytical prediction of the critical load.

4.5. Dimensionless critical loads

Using the dimensionless load $\bar{N} = Nr_0^2/(EI)$ and radius $\hat{R} = R/r_0$ (Section 2.6), the critical loads derived above can be expressed in compact dimensionless form.

4.5.1. Fourier-mode critical loads

The detached-ring limit (Eq. 88) nondimensionalizes to

$$\bar{N}_{\text{cr}}^{\text{det}}(n) = -\frac{(n^2-1)^2}{n^2\,\hat{R}^2}, \qquad n \geq 2, \tag{96}$$

and the full-contact limit (Eq. 89) becomes

$$\bar{N}_{\text{cr}}^{\text{full}}(n) = -\frac{(n^2-1)^2}{n^2\,\hat{R}^2} - \frac{\bar{k}\,\hat{R}^2}{n^2}, \qquad n \geq 2. \tag{97}$$

These two expressions bracket the true critical load for any intermediate contact state and depend on only two dimensionless groups: $\hat{R}$ and $\bar{k}$. The lowest admissible mode $n = 2$ gives $\bar{N}_{\text{cr}}^{\text{det}}(2) = -9/(4\hat{R}^2)$.

4.5.2. Comparison with classical external-pressure ring

For a ring under uniform follower pressure, the classical critical hoop force (Appendix Appendix C) nondimensionalizes to

$$\bar{N}_{\rm cr}^{\rm pressure}(n) = -\frac{n^2-1}{\hat{R}^2}, \qquad n \geq 2. \tag{98}$$

The ratio of the eigenstrain critical load to the pressure critical load is

$$\frac{\bar{N}_{\rm cr}^{\rm det}(n)}{\bar{N}_{\rm cr}^{\rm pressure}(n)} = \frac{n^2-1}{n^2}, \tag{99}$$

which equals 3/4 for $n = 2$ and approaches unity for large n. The eigenstrain-loaded ring buckles at a lower compressive resultant than the pressure-loaded ring because the follower pressure contributes an additional geometric stiffness—the $-p\,w$ term in the area-change functional (Appendix Appendix C)—that is absent when N is a pre-existing internal stress.

4.5.3. Summary

Table 3 collects the dimensionless critical loads for all semi-analytical solutions considered. As mentioned previously, their computation only requires a conventional optimization code or equation solver, and no finite element computation is required. The predictions of these solutions will be demonstrated in Section 5 to be compared with finite element simulations, as validation.

Table 3: Dimensionless critical compressive resultant $\bar{N}_{\rm cr} = N_{\rm cr}\, r_0^2/(EI)$ for a circular ring of dimensionless radius $\hat{R} = R/r_0$.

Model	$\bar{N}_{\rm cr}(n)$	$\bar{N}_{\rm cr}(n=2)$
Detached ring (eigenstrain)	$-\dfrac{(n^2-1)^2}{n^2\hat{R}^2}$	$-\dfrac{9}{4\hat{R}^2}$
External follower pressure	$-\dfrac{n^2-1}{\hat{R}^2}$	$-\dfrac{3}{\hat{R}^2}$
Full contact (eigenstrain, bilateral)	$-\dfrac{(n^2-1)^2}{n^2\hat{R}^2} - \dfrac{\bar{k}\hat{R}^2}{n^2}$	$-\dfrac{9}{4\hat{R}^2} - \dfrac{\bar{k}\hat{R}^2}{4}$

5. Computational Modeling

Finite element simulations are performed using the commercial explicit dynamics code Abaqus/Explicit, which provides robust treatment of the complex contact con-

ditions central to this problem. Thermal expansion serves as the loading mechanism, representing the general eigenstrain framework developed in Section 2.5.

The section is organized in three parts. We first study a circular ring confined by a rigid ring (Section 5.1), for which the analytical ring-limit solutions of Section 4.3 provide a direct benchmark. We then model a one-turn spiral under the same confinement (Section 5.2) and compare the results with the Rayleigh–Ritz estimates of Section 4.1. Finally, we extend the study to multi-turn spirals (Section 5.4), where turn-to-turn self-contact provides intrinsic kinematic locking, and perform a parametric study over thickness and turn number to characterize the onset of inward buckling in the dimensionless parameter space $(\hat{t},\, N_t)$.

5.1. Circular ring confined by a rigid ring

5.1.1. Model description

A circular ring of radius $R = 20$ mm and in-plane thickness $h = 1$ mm is confined by a rigid circular ring of the same radius (Fig. 3(a)). The deformable ring is discretized with two-node Timoshenko beam elements (B21 in Abaqus) and assigned material properties $E = 70$ GPa, $\nu = 0.33$, and thermal expansion coefficient $\alpha = 0.001$ per °C. Thermal loading is applied as a uniform temperature increment ΔT, producing an eigenstrain $\varepsilon^{\text{eigen}} = \alpha\,\Delta T$.

To trigger buckling in the Abaqus/Explicit analysis, a localized inward Gaussian imperfection is prescribed at the crown with an angular extent of 2°. Three dimensionless imperfection amplitudes are considered: $\delta^* = \delta/h = 0.5$, 0.3, and 0.1.

5.1.2. Onset identification criteria

The onset of buckling is identified using three independent criteria, applied to each imperfection amplitude.

The first criterion is energy-based. In the pre-buckling regime, the imposed thermal expansion progressively builds elastic strain energy while the rigid confinement suppresses free expansion; most of the input work is stored as internal (strain) energy and the kinetic energy remains negligible. At the critical temperature, the pre-buckling equilibrium becomes unstable and the structure transitions rapidly to a post-buckled configuration, releasing stored strain energy. A portion of this released energy is temporarily

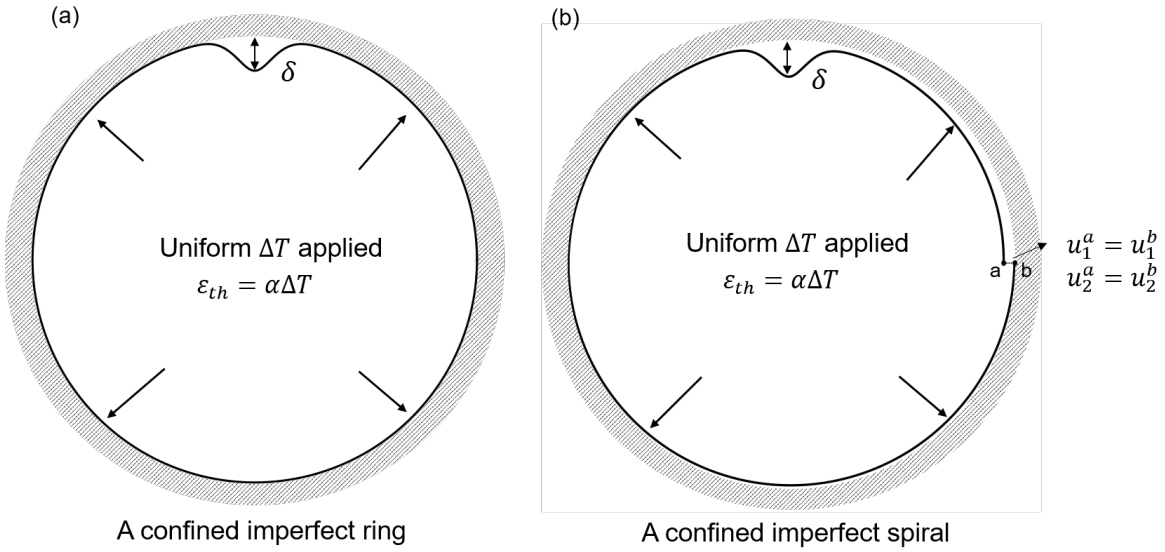

Figure 3: Schematic illustration of the thermally driven confined configurations. (a) A confined imperfect ring subjected to a uniform temperature change ΔT, modeled as a thermal eigenstrain $\varepsilon^{\text{eigen}} = \alpha\,\Delta T$, which induces an outward expansion tendency. The outer rigid wall constrains the expansion and generates contact pressure. (b) A confined imperfect one-turn spiral under the same thermal loading; the spiral opening is stabilized using an equation constraint that couples the two end vertices (enforcing equal in-plane displacements u_1 and u_2) to prevent gap opening and promote stress accumulation.

converted into kinetic energy, producing the characteristic signature of an abrupt drop in internal energy accompanied by a sharp kinetic-energy burst (Fig. 4(a–d)). Similar energy-based onset indicators have been reported in Putelat and Triantafyllidis (2014); Peng and Meguid (2017). After the onset of buckling, the structure evolves toward a stable post-buckling equilibrium path. Therefore, the internal energy approaches a stable plateau, while the kinetic energy remains close to zero after the transient response. Prior to buckling, the ratio KE/IE remains below 5% , confirming that the pre-buckling response is predominantly quasi-static.

The second criterion is force-based. Figure 5(a) shows the dimensionless thermal strain $\alpha\Delta T$ and the normalized hoop force N/EA as functions of ΔT for $\delta^* = 0.1$. In the pre-buckling regime, the two curves nearly coincide, confirming that the imposed eigenstrain is almost entirely converted into elastic mechanical strain and the ring remains effectively fully confined by the rigid boundary. At the critical temperature, a sudden departure from the linear force–strain relation occurs, accompanied by

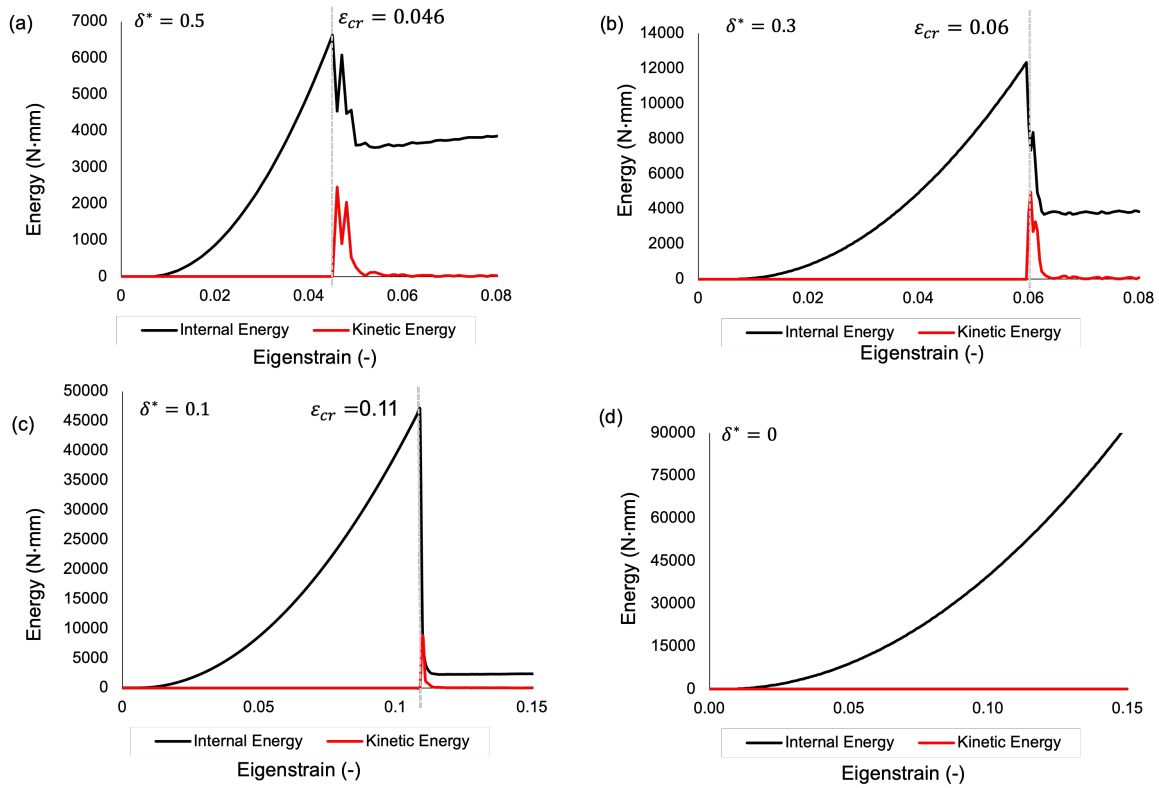

Figure 4: Energy evolution under thermally induced eigenstrain for different dimensionless Gaussian imperfection amplitudes, $\delta^* = \delta/h$. (a–d) Internal energy (black) and kinetic energy (red) versus temperature change for (a) $\delta^* = 0.5$, (b) $\delta^* = 0.3$, (c) $\delta^* = 0.1$, and (d) $\delta^* = 0$. Here, the eigenstrain is varied by changing the imposed temperature field. The imperfection has an angular extent of 2°. The corresponding critical eigenstrains are $\varepsilon_{cr} = 0.046$, 0.06, 0.11, and 0, respectively.

oscillations in N/EA, signaling loss of stability.

The third criterion is mode-based. The radial displacement field is expanded in Fourier harmonics, and the $n = 2$ component—which quantifies ovalization—is tracked over time. Following Kodio et al. (2020), the second-harmonic amplitude is estimated from four equally spaced samples ($\theta = 0$, $\pi/2$, π, $3\pi/2$):

$$A_2(t) \approx \frac{1}{4}\sqrt{\left[u_r(0,t) - u_r(\pi,t)\right]^2 + \left[u_r(\tfrac{\pi}{2},t) - u_r(\tfrac{3\pi}{2},t)\right]^2}. \tag{100}$$

Figure 5(c) shows that A_2 remains negligible throughout the pre-buckling regime and grows sharply at $\Delta T \approx 105.6$ °C, corresponding to $\varepsilon_{\mathrm{cr}} = 0.105$, providing a geometric onset criterion that is independent of force or energy fluctuations and consistent with the other two criteria.

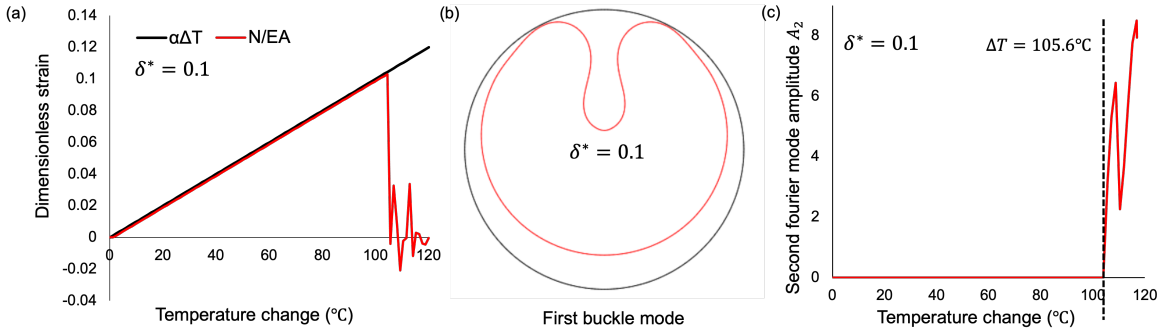

Figure 5: (a) Dimensionless thermal strain $\alpha\Delta T$ (black) and normalized hoop force N/EA (red) versus temperature change for $\delta^* = 0.1$. The near overlap in the pre-buckling regime confirms full confinement. (b) First buckling mode at instability onset, showing asymmetric inward deformation localized near the imperfection. (c) Evolution of the second Fourier-mode amplitude A_2; the sharp growth at $\Delta T \approx 105.6$ °C identifies the buckling onset, corresponding to $\varepsilon_{\mathrm{cr}} = 0.105$.

5.1.3. Results and discussion

The three criteria yield mutually consistent onset eigenstrains for each imperfection amplitude, demonstrating that the identification is robust. The critical eigenstrain levels are $\varepsilon_{cr} = 0.046$, 0.06, and 0.11 for $\delta^* = 0.5$, 0.3, and 0.1, respectively: reducing the imperfection amplitude raises the buckling threshold, bringing the response closer to the theoretical prediction for a perfect ring.

The first buckling mode for $\delta^* = 0.1$ (Fig. 5(b)) exhibits a strongly asymmetric inward deformation localized near the imperfection, rather than a uniform $n = 2$ ovalization, which indicates the imperfection dominated the buckling mode. The imposed geometric imperfection biases the instability toward a non-axisymmetric collapse pattern and suppresses symmetric bifurcation. Nevertheless, the deformation is dominated by the $n = 2$ harmonic, as confirmed by the Fourier tracking, although the imperfection influences the detailed deformation pattern.

The case with zero imperfection does not buckle within the simulated eigenstrain range (Fig. 4(d)). This behavior is consistent with the theoretical prediction that a perfectly symmetric ring does not select a localized buckling mode in the absence of an initial imperfection.

5.1.4. Validation against analytical ring estimates

We now compare the finite-element results with the semi-analytical predictions of Section 4. Two analytical estimates are available for the ring: the Fourier-mode result for a globally detached ring (Eq. 88), and the Glock-type Rayleigh–Ritz estimate with a prescribed detached arc (Eq. 90). Each addresses a different physical regime, and the comparison clarifies which regime the finite-element model captures.

Fourier-mode estimate (global detachment). The detached-ring critical load for mode $n = 2$ (Eq. 88) evaluates to

$$N_{\mathrm{cr}}^{\mathrm{det}}(2) = \frac{9\,EI}{4R^2} = \frac{9 \times 5833.3}{4 \times 400} \approx 32.8 \text{ N/mm}, \tag{101}$$

corresponding to a normalized strain $|N_{\mathrm{cr}}^{\mathrm{det}}|/(EA) \approx 4.7 \times 10^{-4}$, or equivalently $\Delta T_{\mathrm{cr}} \approx 0.47$ °C. The finite-element simulation with $\delta^* = 0.1$ gives $\varepsilon_{\mathrm{cr}} \approx 0.11$ (Fig. 4(c)), more than two orders of magnitude larger. This discrepancy is expected: the Fourier-mode estimate assumes the ring is detached from the wall everywhere and buckles into a global $\cos(2\theta)$ mode, whereas the confined ring in the FE model remains pressed against the rigid wall over nearly the entire circumference until a localized snap-through occurs at the imperfection. The global detached-ring estimate therefore does not apply to the confined, imperfection-triggered instability observed in the simulation.

Glock-type estimate (partial detachment). The Rayleigh–Ritz estimate with a prescribed detached arc (Eq. 90) directly accounts for partial wall contact. However, it requires specifying the detached half-angle ϕ, which depends on the imperfection geometry and is not known *a priori*. One may extract the detached angle from the FE simulation and use it as input to the analytical expression—a consistency check rather than a blind prediction. From the Abaqus results for $\delta^* = 0.1$, the detached half-angle at onset is measured as $\phi \approx 4.55°$ (0.0794 rad). Using the same geometric and material parameters as those adopted in the finite element model, the semi-analytical formulation discussed in section 4.4 predicts

$$N_{\mathrm{cr}}(0.0794) \approx 22850 \text{ N/mm}, \qquad \frac{|N_{\mathrm{cr}}|}{EA} \approx 0.32. \tag{102}$$

The FE simulation yields $N/(EA) \approx 0.11$ (Fig. 5(a)), which is approximately 2.91 times larger than the corresponding value obtained from the finite element simulation.

Additional differences may arise from the idealized kinematic assumptions in the semi-analytical formulation. The theory restricts the admissible deformation to a prescribed inward-only localized mode and treats stretching through a simplified nearly inextensible constraint. The finite element model, however, permits a more general deformation field, including local stretching, contact-induced redistribution, and mode evolution during loading. These additional degrees of freedom reduce the total energy required for buckling and can lower the critical load compared with the semi-analytical estimate.

Figure 6 shows the dependence of the semi-analytical critical load on the effective perturbation half-width ϕ. The predicted critical load decreases rapidly when ϕ increases from a small value, indicating that a highly localized admissible mode produces a large curvature variation and therefore a high bending-energy penalty. As ϕ becomes larger, the admissible mode is allowed to spread over a wider angular region, which reduces the bending contribution and lowers the Rayleigh–Ritz estimate of the critical load. The curve gradually approaches a plateau at large ϕ, suggesting that the semi-analytical prediction is highly sensitive to the prescribed localization width when the mode is strongly confined, but becomes less sensitive once the perturbation is sufficiently spread out. This result explains why using a very small FE-observed localized angle can lead to an overprediction of the critical load: the restricted trial mode over-penalizes bending compared with the more freely evolving deformation mode in the finite element simulation. In addition, the trend shown in this figure is consistent with Fig. 7(b): increasing the effective imperfection or perturbation width of the ring reduces the predicted critical load.

Interpretation. The comparison reveals two distinct instability regimes for the confined ring, summarized in Table 4. When the FE-observed detached angle is substituted into the semi-analytical expression, the predicted critical load is approximately 2.91 times larger than the finite element result. This difference may be mainly attributed to the restricted admissible mode shape, which overestimates the bending energy.

This distinction also has practical implications: in real structures, geometric imperfections and manufacturing defects set the detached region, and the critical load is controlled by the local imperfection geometry rather than by a global energy minimum. The analytical framework developed in Section 4 accommodates both regimes through

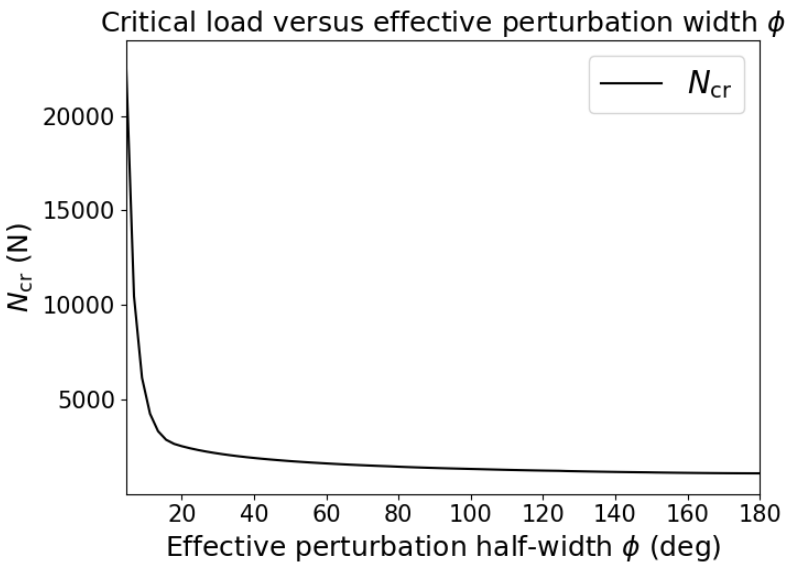

Figure 6: Critical load as a function of the effective perturbation half-width ϕ obtained from the Rayleigh–Ritz formulation. The predicted critical load decreases rapidly as ϕ increases. A highly localized admissible mode imposes large curvature variations within a narrow angular region, which increases the bending-energy contribution and can therefore overestimate the critical load. The curve gradually approaches a plateau for larger ϕ, showing that the critical-load estimate is highly sensitive to the prescribed localization width.

the parameterization by ϕ; the physically relevant value of ϕ must be determined from either the imperfection geometry or a complementary finite-element analysis.

Table 4: Comparison of analytical and FE critical loads for the confined ring ($R = 20$ mm, $h = 1$ mm, $E = 70$ GPa, $\alpha = 0.001/\,^{\circ}\mathrm{C}$).

Model	Detached arc	$\lvert N_{\mathrm{cr}}\rvert/(EA)$	ΔT_{cr} (°C)
Fourier $n = 2$, full detachment	360°	4.7×10^{-4}	0.47
Rayleigh–Ritz at FE-observed ϕ	9.10°	0.32	320
FE ($\delta^* = 0.1$)	$\approx 9.10^{\circ}$	0.11	110

5.2. Spiral confined by a rigid ring

5.3. Model description and FEM results

Following the confined ring model, we next model a one-turn spiral confined by the same rigid ring, as illustrated in Figure 3(b). Because a one-turn open spiral can

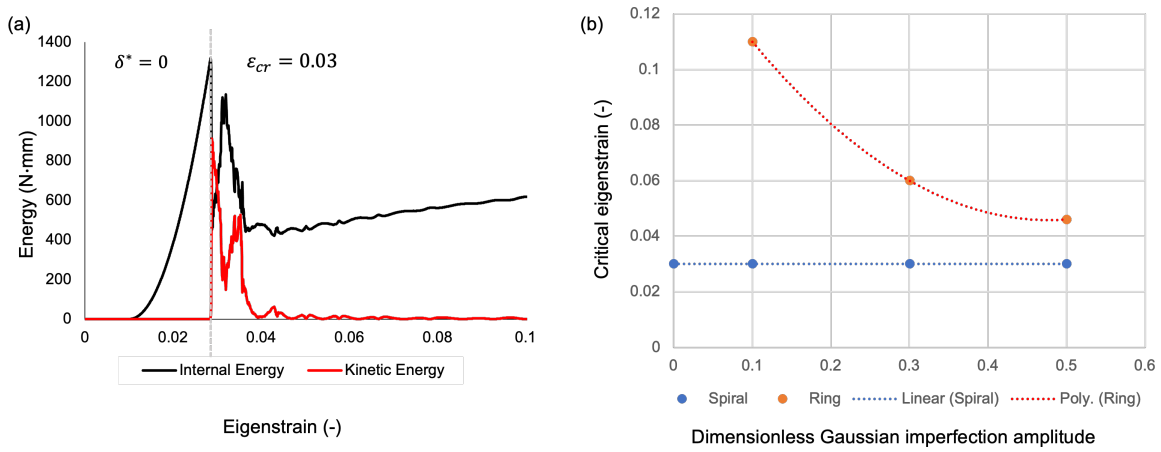

Figure 7: Energy response and critical eigenstrain comparison for the spiral and ring structures. (a) Internal energy and kinetic energy evolution of the spiral structure as a function of eigenstrain for the zero-imperfection case $\delta^* = 0$. A sudden increase in kinetic energy occurs at $\varepsilon_{\mathrm{cr}} \approx 0.03$, indicating the onset of buckling. (b) Critical eigenstrain as a function of the dimensionless Gaussian imperfection amplitude. For the spiral structure, the critical eigenstrain remains approximately constant at $\varepsilon_{\mathrm{cr}} \approx 0.03$, suggesting weak sensitivity to the imperfection amplitude. In contrast, the ring structure shows a strong imperfection sensitivity, where the critical eigenstrain decreases as the imperfection amplitude increases.

partially relieve eigenstrain by end motion, we impose an equal-displacement constraint at the two ends to emulate the kinematic locking that occurs naturally in multi-turn spirals due to turn-to-turn self-contact. The spiral opening is stabilized using an equal displacement constraint that couples the two end nodes, $u_1^a = u_1^b, u_2^a = u_2^b$, thereby preventing end separation, promoting stress accumulation, and enabling buckling. The boundary conditions, loading, and material properties are kept identical to those of the ring case.

The Gaussian imperfection amplitudes were chosen to be consistent with those used in the ring model, with $\delta^* = 0.1$, 0.3, and 0.5. In addition, the zero-imperfection case, $\delta^* = 0$, was also considered as a reference case. As shown in Fig. 7(b), the spiral structure is found to buckle at nearly the same critical eigenstrain over the entire imperfection range $\delta^* = 0$–0.5. This indicates that the critical buckling condition of the spiral is only weakly sensitive to the prescribed Gaussian imperfection amplitude. Unlike the ring, whose buckling response is strongly affected by the presence and magnitude of the initial imperfection, the spiral does not require a large imposed defect to

trigger instability. Instead, the instability is mainly governed by the intrinsic geometry of the spiral itself.

The corresponding energy histories for $\delta^* = 0$–0.5 are also nearly identical. Therefore, for clarity, only one representative energy plot is presented in Fig. 7(a), corresponding to the zero-imperfection case $\delta^* = 0$. The interpretation of the internal energy drop and the kinetic energy burst follows the same physical mechanism as discussed for the imperfect ring. Near the critical eigenstrain, the structure undergoes a sudden transition from the pre-buckling path to the post-buckling deformation mode. During this transition, part of the stored strain energy is released, leading to a decrease in internal energy and a simultaneous transient increase in kinetic energy. After this transient response, the structure evolves toward a stable post-buckling equilibrium state. The internal energy then stabilizes at a nearly constant value, while the kinetic energy decays to approximately zero. In all cases considered here, the ratio between kinetic energy and internal energy remains below 1%. Therefore, the KE/IE ratio is not separately plotted in this figure.

Interestingly, the one-turn spiral can buckle even without an explicitly prescribed geometric imperfection once the opening is stabilized by the equation constraint. This behavior is fundamentally different from that of a closed circular ring. For a perfect circular ring, the geometry is circumferentially symmetric. In the absence of an imposed imperfection, there is no preferred location or direction for the structure to select a localized non-axisymmetric buckling mode. Therefore, the zero-imperfection ring does not buckle within the simulated eigenstrain range. By contrast, a one-turn spiral is not circumferentially uniform. Its curvature, orientation, and boundary configuration vary along the spiral centerline. This non-uniform geometry naturally breaks the circumferential symmetry and provides a preferred pathway for inward deformation. Intuitively, buckling will initiate where the curvature is the smallest. As a result, even without a prescribed Gaussian defect, the spiral geometry itself can initiate an unstable deformation mode under the prescribed eigenstrain loading.

The end constraint also plays an important role in this response. By stabilizing the opening of the spiral, the equation constraint prevents the structure from freely relaxing the imposed thermal eigenstrain through rigid motion or simple opening displacement.

Consequently, stress can accumulate in the spiral as the temperature change increases. Once the stored elastic energy reaches the critical level, the structure readily transitions into an unstable buckling path. Therefore, the spontaneous buckling observed in the zero-imperfection spiral should not be interpreted as being caused by an external defect. Rather, it results from the combined effect of stress accumulation, geometric non-uniformity, and the intrinsic asymmetry of the spiral configuration.

As summarized in Fig. 7(b), the ring and spiral structures exhibit clearly different imperfection sensitivities. The ring does not buckle in the absence of an imposed imperfection because its perfectly symmetric configuration provides no perturbation to break symmetry and activate a non-axisymmetric instability. Once an imperfection is introduced, the response is dominated by the prescribed crown imperfection over the range of amplitudes considered. Moreover, reducing the imperfection amplitude increases the critical temperature change, indicating a higher buckling threshold and bringing the response closer to the ideal ring prediction. Conversely, larger imperfections trigger instability at smaller temperature changes, thereby lowering the critical buckling load and increasing the deviation from the analytical prediction for an ideal ring.

In contrast, the spiral can buckle without any prescribed imperfection and shows only weak sensitivity to small imperfection amplitudes. The nearly constant critical eigenstrain over $\delta^* = 0$–0.5 suggests that the dominant instability mechanism is controlled by the spiral geometry rather than by the imposed initial defect. For small imperfections, the prescribed Gaussian defect mainly affects the detailed local deformation pattern, but it does not significantly alter the critical buckling condition. This further supports the conclusion that the spiral is relatively insensitive to the prescribed imperfection amplitude within the range considered. Its geometric asymmetry can naturally break the symmetry, promote stress localization, and trigger inward buckling even in the absence of an externally imposed imperfection under the prescribed eigenstrain loading.

5.3.1. Validation

By evaluating the semi-analytical solution in Section 4.1.3 using the same parameters as those adopted in the finite element model, the critical load is obtained as

$$N_{\mathrm{cr}}^{\mathrm{analytical}} = 2128 \text{ N}. \tag{103}$$

In comparison, the finite element simulation in section 5.2 gives the following

$$N_{\mathrm{cr}}^{\mathrm{FEM}} = 2100 \text{ N}, \tag{104}$$

corresponding to a critical eigenstrain of

$$\varepsilon_{\mathrm{cr}} = 0.03. \tag{105}$$

The relative difference between the semi-analytical prediction and the finite element result is

$$\frac{\left|N_{\mathrm{cr}}^{\mathrm{analytical}} - N_{\mathrm{cr}}^{\mathrm{FEM}}\right|}{N_{\mathrm{cr}}^{\mathrm{FEM}}} \times 100\% = \frac{|2128 - 2100|}{2100} \times 100\% \approx 1.33\%. \tag{106}$$

The small discrepancy indicates good agreement between the finite element model and the theoretical formulation.

The first mode shape comparison is shown in Fig. 8. Figure 8(a) shows the centerline predicted by the semi-analytical formulation, while Fig. 8(b) shows the corresponding mode shape obtained from the finite element simulation. Although the two results are represented differently, both exhibit a similar inward-kinked deformation pattern. This agreement suggests that the semi-analytical formulation captures the dominant deformation mode observed in the finite element simulation.

Although the deformation visually appears as an inward bending mode, the stretching contribution cannot be determined from the centerline shape alone. Therefore, the axial stretching measure

$$S = \frac{u_{,\theta}}{J} + \kappa w \tag{107}$$

was evaluated quantitatively. The resulting non-negligible value of

$$\frac{U_s}{U_b} \approx 10 \tag{108}$$

indicates that the first inward mode involves significant axial stretching and should be interpreted as a constrained bending–stretching mode. The structure can only be regarded as nearly inextensible before the critical point. After buckling occurs, stretching energy is still present, as also shown in Fig. 5(a).

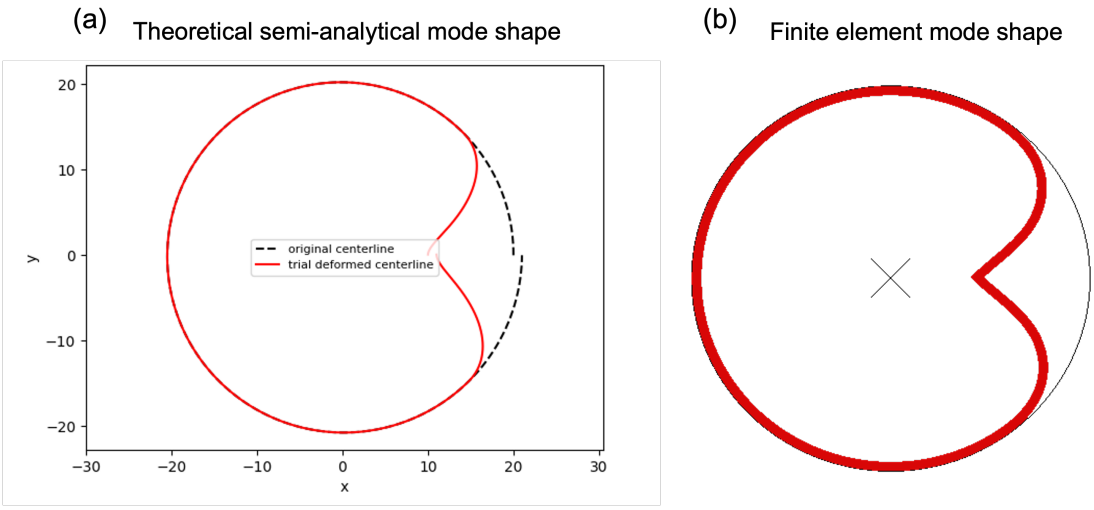

Figure 8: Comparison between the theoretical semi-analytical mode shape and the finite element mode shape for the inward kinked spiral deformation. Panel (a) shows the trial deformed centerline predicted by the semi-analytical formulation, while panel (b) shows the corresponding mode shape obtained from finite element analysis(solid element).

5.4. Parametric study

In multi-turn spirals, adjacent turns are in self-contact, which suppresses relative sliding and opening between layers. This turn-to-turn interaction introduces intrinsic kinematic locking and allows the thermally induced eigenstrain to be converted into compressive resultants without imposing artificial equal-displacement end constraints. Therefore, the multi-turn spiral is treated as a physically relevant layered-structure limit and is used to assess how geometric parameters control inward buckling.

To better understand the effect of geometry, we perform a parametric study by varying the layer thickness, inner radius, and number of turns. In the self-contact configuration, the pitch is taken to be equal to the layer thickness, i.e.,

$$D = t, \tag{109}$$

so that neighboring turns remain in contact without a gap.

To facilitate comparison across different geometries, all lengths are nondimensionalized by the initial inner radius r_0, defined as the radius at $\theta = 0$. The dimensionless thickness is defined as

$$\hat{t} = \frac{t}{r_0}, \tag{110}$$

and the number of turns is denoted by N_t. Under the self-contact condition $D = t$, the outer radius is given by

$$r_{\text{out}} = r_0 + N_t t, \tag{111}$$

or, equivalently,

$$\hat{r}_{\text{out}} \equiv \frac{r_{\text{out}}}{r_0} = 1 + N_t \hat{t}. \tag{112}$$

Therefore, the multi-turn self-contact geometry can be characterized by the two independent dimensionless parameters $(\hat{t}, N_t)$.

To isolate the effect of the number of turns, the outer radius r_{out} is fixed as the reference length while the thickness ratio is held constant at $\hat{t} = 0.047$. The inner radius is then adjusted according to the self-contact relation

$$\hat{r}_{\text{out}} = \hat{r}_0 + N_t \hat{t}, \tag{113}$$

which ensures geometrically consistent comparisons for different values of N_t.

The resulting instability is driven by the geometric confinement and kinematic coupling induced by turn-to-turn self-contact. In contrast, a single-turn spiral does not provide such interlayer constraints and therefore does not buckle under the same loading unless additional boundary constraints are imposed, as discussed in the previous section.

The parametric study shows that the inward buckling threshold is strongly affected by both the dimensionless thickness and the number of turns(Fig 9). A larger dimensionless thickness increases the bending resistance of the spiral layers, leading to a higher critical temperature. Similarly, increasing the number of turns generally enhances turn-to-turn self-contact, which strengthens geometric confinement and kinematic coupling between adjacent layers. A slight deviation is observed at $N_t = 8$, where the critical temperature is approximately 126°C (eigenstrain of 0.126). This local discrepancy may result from a change in the active contact configuration or a transition in the dominant buckling mode. Since the instability of a self-contacting spiral is strongly affected by which turns are in contact and where stress localizes, small changes in contact evolution can lead to a non-monotonic point in the critical temperature curve. Numerical factors, including mesh resolution, contact discretization, and the threshold used to identify buckling onset, may also contribute to this deviation. Nevertheless, the over-

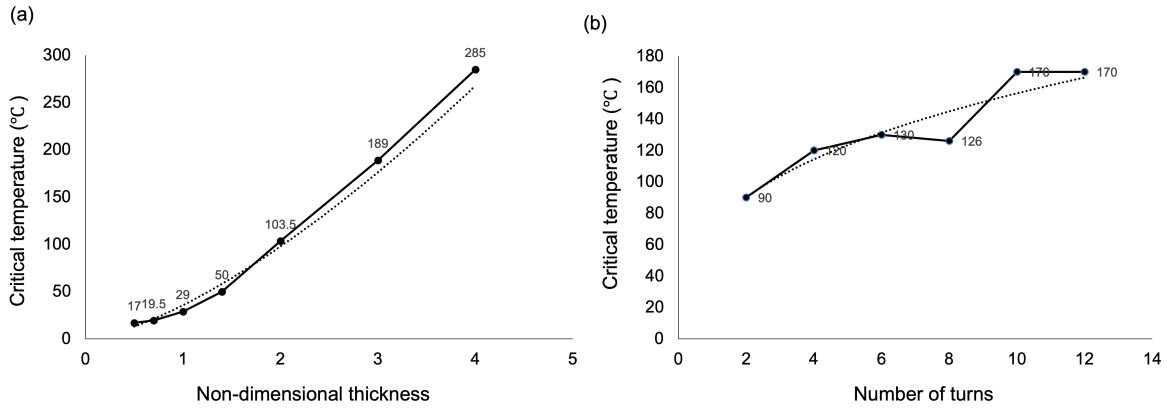

Figure 9: Parametric study of inward buckling in multi-turn self-contact spiral structures. The dashed lines represent power-law fits to the two curves, highlighting the scaling trend of the critical load with respect to the geometric parameter. (a) Critical temperature versus dimensionless thickness $\hat{t} = t/r_0$. A larger thickness increases the critical temperature, indicating stronger resistance to inward buckling. (b) Critical temperature versus number of turns N_t for fixed outer radius and constant $\hat{t} = 0.047$. Increasing the number of turns enhances turn-to-turn self-contact, geometric confinement, and stress accumulation, leading to a higher buckling threshold. These results indicate that the critical buckling condition is controlled by the dimensionless thickness and the self-contact configuration of the multi-turn spiral.

all trend indicates that increasing the number of turns promotes stress accumulation and generally raises the buckling threshold. Therefore, the instability of the multi-turn spiral is governed by the combined effects of layer stiffness, self-contact, and geometric confinement.

It is also worth noting that the two increasing trends have different characteristics. The critical temperature increases rapidly with dimensionless thickness, showing a nearly exponential dependence, whereas the effect of the number of turns appears to gradually approach a plateau. This suggests that thickness directly strengthens the bending resistance, while additional turns may eventually provide limited extra confinement once the main self-contact region has formed. The lower value at $N_t = 8$ may arise from a local change in contact configuration, a mode transition, or numerical sensitivity. Further parametric studies are required to clarify whether the turn-number plateau is a physical saturation behavior or a result of model resolution and contact evolution.

6. Discussions

6.1. Complementarity conditions for contact mechanism

Throughout the analytical development we represent wall contact by a penalty stiffness k with a Heaviside activation (Eq. 39). This regularization is what makes the closed-form critical load $N_{\mathrm{cr}}(n)$ and its mode scaling (Eq. 87) possible. The physically exact description, however, is unilateral (Signorini) contact, which is governed by a complementarity condition rather than a smooth penalty:

$$g(\theta) \geq 0, \qquad \lambda(\theta) \geq 0, \qquad \lambda(\theta)\, g(\theta) = 0. \tag{114}$$

Here $g(\theta) = -w(\theta)$ is the gap between the structure and the rigid wall, and $\lambda(\theta)$ is the normal contact reaction. The first condition states that the gap cannot be negative, since the spiral or ring cannot cross the outer wall. The second states that the reaction cannot be negative, since a frictionless rigid wall can push on the structure but cannot pull it. The third is the complementarity condition itself, which couples the two: where the structure is separated from the wall ($g > 0$), the reaction must vanish ($\lambda = 0$), so no force is transmitted across a gap; where the structure is in contact ($g = 0$), the reaction may be positive, supplying whatever compressive traction is needed to prevent penetration. Together these three conditions enforce the correct no-penetration physics without prescribing in advance which portions of the boundary are in contact.

The corresponding equilibrium statement is

$$\mathcal{L}[w] + J\,\lambda = 0, \tag{115}$$

where, for the spiral, the operator $\mathcal{L}$ collects the membrane and bending contributions of the normal equilibrium equation (44),

$$\mathcal{L}[w] = -\left(N\,\kappa\,J + \frac{d}{d\theta}\left(\frac{N}{J}\,w_\theta\right)\right) + \left(J\,M\,\kappa^2 + \frac{d}{d\theta}\left(\frac{1}{J}\,M_\theta\right)\right). \tag{116}$$

The essential difficulty is that the contact set is not known beforehand: it is part of the solution. Under the strict inward constraint $w(\theta) \leq 0$ (equivalently $g \geq 0$), a pure global Fourier mode $w = A\cos(n\theta)$ is no longer admissible, because such a mode contains both inward and outward excursions and the outward lobes would penetrate the wall. The admissible field is therefore restricted to inward and locally detached deformation, and the stability problem becomes a variational inequality with an unknown active set.

Solving this variational inequality directly lies beyond the scope of the present analytical treatment. We therefore adopt the penalty regularization throughout, which relaxes the hard constraint into a one-sided elastic foundation and recovers the closed-form expressions used in Section 4. The penalty model permits a small, controlled overclosure in place of the exact reaction λ, and reproduces the complementarity behaviour in the limit of large k.

6.2. Fundamental differences in the mechanical behavior of spirals and rings

A circular ring may be viewed as the geometric limit of a one–turn spiral in which the radial increment vanishes. In this limit the radius becomes independent of the circumferential coordinate,

$$r(\theta) = a + b\theta \quad \longrightarrow \quad R \qquad (b \to 0),$$

and therefore

$$J(\theta) = \sqrt{r^2 + b^2} \;\longrightarrow\; R,$$

which is constant. From a purely geometric perspective, the ring may therefore be regarded as a special case of the spiral with constant metric coefficient J.

However, despite this geometric connection, the two problems are fundamentally different from a mechanical standpoint because their boundary conditions are not equivalent. A spiral is an open curve defined on $\theta \in [0, 2\pi]$ with two physical ends, whereas a ring is a closed structure satisfying periodic boundary conditions,

$$w(0) = w(2\pi), \qquad w'(0) = w'(2\pi).$$

Consequently, even in the limit $b \to 0$, the spiral problem does not strictly reduce to the classical ring problem. Instead, the spiral approaches the behavior of an open circular arc with constant curvature. Only after imposing periodic boundary conditions does the classical closed-ring model emerge.

Another essential distinction lies in the spatial distribution of curvature. In a circular ring the curvature is uniform,

$$\kappa = \frac{1}{R},$$

which preserves full circumferential symmetry. By contrast, an Archimedean spiral exhibits a non-uniform curvature distribution,

$$\kappa(\theta) = \frac{r^2 + 2b^2}{(r^2 + b^2)^{3/2}},$$

so that the structural stiffness varies along the circumferential direction, as illustrated in 10. This intrinsic geometric inhomogeneity breaks the rotational symmetry of the system and provides a natural mechanism for symmetry breaking in the post-buckling response.

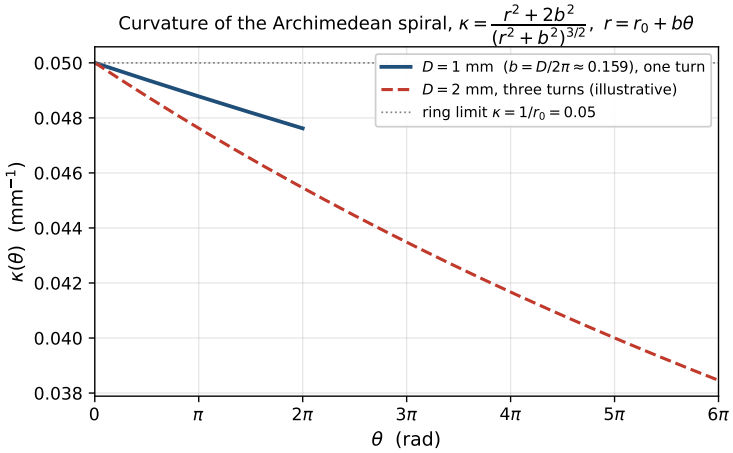

Figure 10: Spiral curvature κ as a function of θ.

These geometric and boundary-condition differences strongly influence how compressive stresses develop under volumetric expansion loading. In a spiral, the open ends together with possible interlayer interactions in a multilayer coil restrict the natural radial expansion induced by eigenstrain. The resulting incompatibility generates compressive stresses along the spiral centerline, which can drive the structure toward an unstable equilibrium configuration. Because the spiral lacks circumferential symmetry, this instability can emerge spontaneously even in the absence of a prescribed geometric imperfection.

By contrast, in a closed ring the compressive stress arises from the kinematic constraint associated with the closed-loop geometry: uniform thermal expansion cannot be accommodated without developing in-plane compressive forces along the ring. Nevertheless, the ring retains perfect circumferential symmetry, and therefore classical ring

buckling is characterized by symmetric Fourier modes determined by the wave number n.

These observations highlight that, although the spiral and the ring are geometrically related, their mechanical behavior is fundamentally governed by different symmetry and boundary-condition constraints. As a result, the spiral exhibits a richer instability behavior that is absent in the classical closed-ring problem.

For reference, a multilayer configuration composed of concentric rings may be regarded as an idealized counterpart of the spiral architecture. In such a system each layer forms a closed loop with uniform curvature and satisfies periodic boundary conditions along the circumferential direction. As a result, the structure preserves full circumferential symmetry and instability typically develops through global Fourier modes of the ring. By contrast, the spiral geometry introduces both curvature variation and open-ended boundaries, which break this symmetry and allow stress to redistribute non-uniformly along the structure. This geometric asymmetry promotes localized instability modes and provides a natural mechanism for the inward collapse observed in spiral structures.

6.3. Comparison with the ring under external pressure

It is instructive to contrast the eigenstrain-driven critical load with the classical result for a ring buckling under external pressure, since the two are algebraically similar yet arise from different loading mechanics.

Consider a thin circular ring under uniform external hydrostatic pressure p that remains normal to the surface (a follower load). Under the small-deformation assumption, pre-buckling shear and bending effects are negligible, and local equilibrium gives a direct relation between the circumferential membrane (hoop) force N and the applied pressure,

$$N \approx pR. \tag{117}$$

The onset of instability is governed by the critical hoop force

$$N_{\mathrm{cr}} = \frac{EI}{R^2}\,(n^2 - 1), \qquad n \geq 2, \tag{118}$$

or equivalently, using Eq. (117), the classical critical pressure (Timoshenko and Gere,

2012)

$$p_{\mathrm{cr}} = \frac{EI}{R^3}\,(n^2 - 1). \tag{119}$$

Here n is the buckling mode number; the restriction $n \geq 2$ applies because $n = 1$ corresponds to a rigid-body translation of the ring with no change in cross-sectional shape or internal strain.

The pressure result (118) is closely analogous to the detached-ring eigenstrain result (88): in both, N is the internal hoop force at the onset of buckling. The two differ, however, by the mode-dependent factor

$$\frac{N_{\mathrm{cr}}^{\mathrm{eigen}}(n)}{N_{\mathrm{cr}}^{\mathrm{pressure}}(n)} = \frac{(n^2-1)^2/n^2}{n^2-1} = \frac{n^2-1}{n^2}, \tag{120}$$

which equals $3/4$ at $n = 2$ and approaches unity for large n. The origin of this difference is the nature of the load. External pressure is a follower load that remains normal to the deformed ring, so it does additional work through the change in enclosed area as the ring deflects. This contributes an extra geometric term $-p\,w$ to the governing equation (Appendix Appendix C, Eq. C.10), which lowers the resistance to buckling and thereby raises the critical hoop force relative to the eigenstrain case. By contrast, the eigenstrain-induced hoop force in our formulation is a pre-existing internal stress generated by constrained expansion under full confinement; it does not vary with the deformed radius, so the $-p\,w$ contribution is absent. The eigenstrain-loaded ring therefore buckles at a lower hoop force than the pressure-loaded ring at the same mode number.

6.4. Role of imposed end constraints for spiral

A fundamental difference between an Archimedean spiral and a circular ring is that the spiral is naturally an open curve with two free ends. Under imposed expansion, a free-standing spiral can partially relax the deformation through end motion, sliding, or radial unwinding. Therefore, it does not necessarily accumulate large circumferential compressive stress in the same manner as a closed ring, unless additional resistance mechanisms, such as interlayer friction, adhesion, external confinement, or end constraints, inhibit this free relaxation. In the present study, we intentionally impose end constraints in both the theoretical formulation and the finite-element simulations to isolate the stress accumulation mechanism. These constraints idealize situations in which

the spiral cannot freely unwind or expand due to surrounding mechanical restrictions. As a result, part of the imposed eigenstrain is converted into elastic strain, leading to the build-up of compressive hoop stress and eventually driving inward buckling. Thus, the instability analyzed here should be interpreted as the response of a constrained spiral, rather than that of a completely free-standing spiral.

6.5. Discussion of inextensibility

If strict inextensibility before buckling is imposed, the tangential and normal displacements must satisfy the inextensibility condition

$$\frac{1}{J}\frac{du}{d\theta} + \kappa w = 0, \tag{121}$$

where $u(\theta)$ is the tangential displacement, $w(\theta)$ is the normal displacement, $J(\theta)$ is the arc-length metric, and $\kappa(\theta)$ is the curvature of the spiral centerline. Integrating Eq. (121) from 0 to θ gives

$$u(\theta) = -\int_0^\theta \kappa(\eta) J(\eta) w(\eta)\, d\eta + C, \tag{122}$$

where $C = u(0)$ is an integration constant. In the present formulation, the end constraint

$$u(2\pi) = u(0) \tag{123}$$

is imposed to enable stress accumulation in the spiral and to maintain consistency with the boundary conditions used in the subsequent finite-element simulations. Combining Eqs. (122) and (123) gives an additional compatibility constraint on the normal displacement,

$$\int_0^{2\pi} \kappa(\theta) J(\theta) w(\theta)\, d\theta = 0. \tag{124}$$

This condition means that the curvature-weighted average normal displacement must vanish. For a circular ring, where κ and J are constants, Eq. (124) reduces to

$$\int_0^{2\pi} w(\theta)\, d\theta = 0. \tag{125}$$

Therefore, if $w(\theta)$ is restricted to be non-positive everywhere, i.e.,

$$w(\theta) \leq 0, \tag{126}$$

then Eq. (125) can only be satisfied by the trivial solution

$$w(\theta) = 0. \tag{127}$$

This shows that strict inextensibility, periodic tangential displacement, and an inward-only normal displacement cannot generally be satisfied simultaneously. In other words, a truly inextensible closed ring or spiral would require $w(\theta)$ to contain both inward and outward components so that the weighted average displacement is zero. Since the present problem also includes a rigid outer wall, outward displacement is geometrically restricted by the non-penetration condition. Therefore, instead of enforcing the strict inextensibility condition exactly, we include the stretching energy and minimize the total energy with respect to the admissible displacement field. In this way, the structure is treated as nearly inextensible: stretching is energetically penalized, but the constraint $du/Jd\theta + \kappa w = 0$ is not imposed exactly.

7. Conclusions

In this paper, we developed a theoretical and finite-element framework for the inward buckling of spiral layered structures subjected to volumetric expansion and external confinement. The imposed thermal or chemical eigenstrain was converted into a compressive tangential resultant when the free expansion of the spiral was restricted by geometric confinement, end constraints, or inter-layer interactions. This eigenstrain-to-compression mechanism provides the driving force for inward instability.

To benchmark the spiral model, we compared it with its limiting case: a circular ring obtained by setting the radial increment per revolution to zero, so that the centerline radius becomes constant. This reduction removes the geometric non-uniformity of the Archimedean spiral and isolates the roles of curvature, confinement, and contact constraints. Under the same loading and boundary conditions, the ring response serves as a baseline for validating the formulation and for interpreting how the spiral geometry modifies the effective stiffness and stress distribution. In particular, increasing the number of turns introduces additional geometric confinement and inter-layer interactions, which redistribute the compressive stress and alter the instability threshold relative to the ideal ring limit.

The analysis shows that contact plays a central role in determining the buckling threshold. Compared with a freely deforming or globally detached ring, contact with the rigid wall greatly increases the critical load because it restricts the admissible deformation shape. The wall prevents outward motion and limits the structure to inward or locally detached deformation modes. As a result, the structure cannot adopt the energetically favorable global sinusoidal buckling mode, and a much larger compressive load is required to trigger instability. In this sense, contact does not simply add a local reaction force; it fundamentally changes the admissible displacement field and raises the critical buckling load.

The contact energy term was retained in the general energy formulation to facilitate future extensions to multilayer spiral structures. For the single-layer case with an ideal rigid outer wall and frictionless unilateral contact, the contact contribution may be taken as zero because no elastic energy is stored in the rigid wall. In this case, the effect of contact is imposed through the admissible displacement constraint rather than through an explicit elastic energy term. However, in a multilayer spiral, neighboring layers can come into contact with each other. Such inter-layer contact can generate additional penalty energy, restrict relative layer motion, and modify the admissible deformation field. Therefore, although the contact energy term is not active in the present ideal rigid-wall formulation, retaining it provides a more general framework for describing inter-layer contact effects in practical multilayer configurations.

The ring limit also highlights the limitation of global imperfection or global Fourier-mode assumptions. For a confined ring, a global sinusoidal imperfection is not physically admissible once the rigid wall is present, because the wall restricts the outward part of the mode. Therefore, the buckling mode cannot be treated as a fully global deformation around the entire circumference. Instead, the instability must be described using a local imperfection or a localized detached region, where inward deformation initiates near the defect and then evolves into a snap-through-like collapse. This explains why the confined ring exhibits strong sensitivity to local imperfection geometry, while the spiral can buckle through its own geometric asymmetry, turn-to-turn constraint, and stress localization.

The role of inextensibility was also clarified. In the inextensible approximation, the

tangential strain of the perturbation is taken to be zero, so the deformation does not store additional stretching energy during the linearized buckling calculation. Under this condition, the imposed eigenstrain cannot be accommodated as free extension; instead, it is transferred into elastic strain and therefore into compressive stress. Thus, the inextensible assumption removes the perturbation stretching energy from the Rayleigh–Ritz estimate, while the constrained eigenstrain remains the source of the compressive resultant that drives buckling.

Overall, the results demonstrate that inward buckling of confined spiral and ring structures is governed by the combined effects of eigenstrain-induced compression, unilateral contact, geometric confinement, and imperfection localization. Contact substantially increases the critical load by restricting the deformation shape, while the rigid wall makes global ring imperfections inappropriate and requires a local imperfection-based description. These findings provide a mechanics-based explanation for localized inward collapse in spiral layered structures and establish a foundation for predicting buckling thresholds in practical confined multilayer systems.

Acknowledgments

This research was supported by the U.S. National Science Foundation through grant CMMI-2543158 and by the Center for Battery Sustainability of MIT and Northeastern University. The authors thank Dr. Juan Hurtado of Dassault Systemes Simulia Corp. for the technical advice on simulations, Dr. Wei Li of Northeastern University for the constructive comments, and Dr. Wei Li of Stony Brook University for the inspiring discussions when formulating this research.

Author contributions: CRediT

Xinran Shi: Data curation; Formal analysis; Investigation; Methodology; Software; Validation; Visualization; Writing – original draft. **Juner Zhu:** Conceptualization; Methodology; Project administration; Resources; Validation; Writing – review & editing; Formal analysis; Funding acquisition.

Appendix A. First variation of the total potential energy

The first variation of the stretching energy is given by

$$\begin{aligned}
\delta U_{\text{stretching}} &= EA \int_0^{2\pi N_t} \varepsilon_{tt}^{\text{elastic}}\, \delta\varepsilon_{tt}^{\text{elastic}}\, J\, d\theta \\
&= EA \left[\varepsilon_{tt}^{\text{elastic}}\, \delta u \Big|_0^{2\pi N_t} + \varepsilon_{tt}^{\text{elastic}}\, \frac{1}{J} \frac{dw}{d\theta}\, \delta w \Big|_0^{2\pi N_t} \right] \\
&\quad - EA \int_0^{2\pi N_t} \frac{d\varepsilon_{tt}^{\text{elastic}}}{d\theta}\, \delta u\, d\theta \\
&\quad - EA \int_0^{2\pi N_t} \left[\varepsilon_{tt}^{\text{elastic}} \kappa J + \frac{d}{d\theta} \left(\varepsilon_{tt}^{\text{elastic}}\, \frac{1}{J} \frac{dw}{d\theta} \right) \right] \delta w\, d\theta.
\end{aligned} \tag{A.1}$$

Similarly, taking the variation of bending energy, we obtain

$$\begin{aligned}
\delta U_{\text{bending}} &= EI \left[(\tilde{\kappa} - \kappa)\, \frac{1}{J} \frac{d(\delta w)}{d\theta} \Big|_0^{2\pi n} - \frac{1}{J} \frac{d(\tilde{\kappa} - \kappa)}{d\theta}\, \delta w \Big|_0^{2\pi N_t} \right] \\
&\quad + EI \int_0^{2\pi N_t} (\tilde{\kappa} - \kappa)\, \frac{d\kappa}{d\theta}\, \delta u\, d\theta \\
&\quad + EI \int_0^{2\pi N_t} \left[J(\tilde{\kappa} - \kappa)\, \kappa^2 + \frac{d}{d\theta} \left(\frac{1}{J} \frac{d(\tilde{\kappa} - \kappa)}{d\theta} \right) \right] \delta w\, d\theta.
\end{aligned} \tag{A.2}$$

Finally, taking the variation of the contact energy, we obtain

$$\delta \Pi_{\text{contact}} = \int_0^{2\pi N_t} k\, H(w)\, w\, J\, \delta w\, d\theta. \tag{A.3}$$

Collecting the coefficients of δu and δw yields the governing equations and natural boundary conditions. Enforcing $\delta U_{\text{total}} = 0$ for arbitrary variations δu and δw yields the governing equations and natural boundary conditions.

$$
\begin{aligned}
\delta U_{\text{total}} &= \underbrace{EA\int_0^{2\pi N_t} \varepsilon_{tt}^{\text{elastic}}\,\delta\varepsilon_{tt}^{\text{elastic}}\,J\,d\theta}_{\text{stretching}} + \underbrace{EI\int_0^{2\pi N_t} (\tilde{\kappa}-\kappa)\,\delta\tilde{\kappa}\,J\,d\theta}_{\text{bending}} + \underbrace{\int_0^{2\pi N_t} k\,H(w)\,w\,J\,\delta w\,d\theta}_{\text{contact}} \\
&= \left[EA\,\varepsilon_{tt}^{\text{elastic}}\,\delta u + EA\,\varepsilon_{tt}^{\text{elastic}}\frac{1}{J}w_\theta\,\delta w + EI\,(\tilde{\kappa}-\kappa)\frac{1}{J}\delta w_\theta - EI\,\frac{1}{J}(\tilde{\kappa}-\kappa)_\theta\,\delta w\right]_0^{2\pi N_t} \\
&\quad + \int_0^{2\pi N_t}\Bigg\{\Big[-EA(\varepsilon_{tt}^{\text{elastic}})_\theta + EI(\tilde{\kappa}-\kappa)\,\kappa_\theta\Big]\,\delta u \\
&\quad + \Big[-EA\Big(\varepsilon_{tt}^{\text{elastic}}\kappa J + \frac{d}{d\theta}\Big(\varepsilon_{tt}^{\text{elastic}}\frac{1}{J}w_\theta\Big)\Big) + EI\Big(J(\tilde{\kappa}-\kappa)\kappa^2 + \frac{d}{d\theta}\Big(\frac{1}{J}(\tilde{\kappa}-\kappa)_\theta\Big)\Big) \\
&\quad + k\,H(w)\,w\,J\Big]\,\delta w\Bigg\}\,d\theta.
\end{aligned}
\tag{A.4}
$$

Appendix B. Reduce to a circular ring

When a spiral reduce to a circular ring. We have,

$$
\kappa = \frac{1}{R}, \quad \kappa_\theta = 0, \quad J = R. \tag{B.1}
$$

For tangential equilibrium equation (41), when $\kappa_\theta = 0$, it reduces to,

$$
N_\theta = 0 \tag{B.2}
$$

For normal equilibrium equation (42), along with (B.2), it can be reduce to,

$$
-\left(N + \frac{N}{R}w_{\theta\theta}\right) + \left(\frac{M}{R} + \frac{1}{R}M_{\theta\theta}\right) + kRH(w)\,w = 0. \tag{B.3}
$$

Together with equation(29), we can obtain:

$$
-\left(N + \frac{Nw_{\theta\theta}}{R}\right) + \frac{EI}{R^3}\left(w_{\theta\theta\theta\theta} + 2w_{\theta\theta} + w\right) + kRH(w)\,w = 0. \tag{B.4}
$$

For the buckling analysis, we focus on small perturbations about the base state $w(\theta)$. The constant term N is absorbed into the base-state equilibrium and therefore eliminated from the perturbation equation, yielding,

$$
-\frac{Nw_{\theta\theta}}{R} + \frac{EI}{R^3}\left(w_{\theta\theta\theta\theta} + 2w_{\theta\theta} + w\right) + kRH(w)\,w = 0. \tag{B.5}
$$

Appendix C. Buckling of a circular ring under uniform follower pressure: energy derivation

We consider a thin circular ring of radius R and bending rigidity EI subjected to a uniform external pressure p that remains normal to the *deformed* ring (follower pressure). The kinematics is described by the in-plane displacement field

$$\boldsymbol{x}(\theta) = \boldsymbol{X}(\theta) + u(\theta)\,\boldsymbol{t}(\theta) + w(\theta)\,\boldsymbol{n}(\theta), \qquad \theta \in [0, 2\pi], \tag{C.1}$$

where u and w denote the tangential and radial displacements, respectively. For a circular ring, $ds = R\,d\theta$ and $\kappa = 1/R$.

Appendix C.1. Total potential energy

The total potential energy is written as

$$\Pi[w] \;=\; U_b[w] \;+\; \Pi_p[w], \qquad \Pi_p[w] = -p\,\Delta A[w], \tag{C.2}$$

where U_b is the bending energy and Π_p is the pressure potential energy, expressed in terms of the change of the enclosed area ΔA.

Appendix C.2. Bending energy

Using the curvature variation for a circular ring,

$$\Delta\kappa \equiv \tilde{\kappa} - \kappa = -\frac{1}{R^2}\big(w + w_{\theta\theta}\big), \tag{C.3}$$

the bending energy is

$$U_b[w] = \frac{1}{2}\int_0^{2\pi} EI\,(\Delta\kappa)^2\,ds = \frac{1}{2}\int_0^{2\pi} \frac{EI}{R^3}\big(w + w_{\theta\theta}\big)^2\,d\theta. \tag{C.4}$$

Appendix C.3. Pressure potential energy

For a closed planar curve, the enclosed area is $A = \frac{1}{2}\int_0^{2\pi}(xy_\theta - yx_\theta)\,d\theta$. A standard small-deformation expansion about the circular base configuration yields the area change (up to second order) as

$$\Delta A[w] \;=\; \int_0^{2\pi}\left(R\,w + \frac{1}{2}w^2 + \frac{1}{2}w_\theta^2\right)d\theta + (\text{terms involving } u \text{ and higher-order terms}). \tag{C.5}$$

In the linear buckling analysis, only the terms that contribute to the first variation about the circular base state are needed, which lead to the pressure contribution

$$\Pi_p[w] = -p\,\Delta A[w] \;\Rightarrow\; \delta\Pi_p = -p\int_0^{2\pi} (\delta w + w\,\delta w + w_\theta\,\delta w_\theta)\,d\theta. \tag{C.6}$$

Integrating the last term by parts and noting periodicity ($\delta w(0) = \delta w(2\pi)$, $\delta w_\theta(0) = \delta w_\theta(2\pi)$), we obtain

$$\delta\Pi_p = -p\int_0^{2\pi} (\delta w + w\,\delta w - w_{\theta\theta}\,\delta w)\,d\theta = -p\int_0^{2\pi} (1 + w - w_{\theta\theta})\,\delta w\,d\theta. \tag{C.7}$$

The constant term corresponds to the axisymmetric base-state equilibrium and is absorbed into the base configuration. Therefore, the linearized pressure contribution to the buckling equation is

$$\delta\Pi_p \;\Rightarrow\; -p\int_0^{2\pi} (w + w_{\theta\theta})\,\delta w\,d\theta. \tag{C.8}$$

Appendix C.4. Stationarity and governing equation

Taking the first variation of U_b from (C.4) gives

$$\delta U_b = \int_0^{2\pi} \left[-\frac{EI}{R^3}\,(w_{\theta\theta\theta\theta} + 2w_{\theta\theta} + w)\right]\delta w\,d\theta, \tag{C.9}$$

where periodic boundary terms vanish. Enforcing stationarity $\delta\Pi = \delta U_b + \delta\Pi_p = 0$ for arbitrary δw yields the linear buckling equation for a circular ring under uniform follower pressure:

$$-p\,(w + w_{\theta\theta}) - \frac{EI}{R^3}\,(w_{\theta\theta\theta\theta} + 2w_{\theta\theta} + w) = 0. \tag{C.10}$$

Appendix C.5. Critical pressure

Assuming a sinusoidal mode $w(\theta) = W\cos(n\theta)$ ($n \geq 2$), substituting into (C.10) gives the classical result

$$p_{\mathrm{cr}} = \frac{EI}{R^3}(n^2 - 1). \tag{C.11}$$

References

Bhattacharya, S., Demirci, H.E., Nikitas, G., Prakhya, G.K.V., Lombardi, D., Alexander, N.A., Aleem, M., Amani, S., Mylonakis, G., 2021. Physical modeling of interaction problems in geotechnical engineering, in: Modeling in Geotechnical Engineering. Elsevier, pp. 205–256.

Bongtae Han, Yifan Guo, 1996. Determination of an effective coefficient of thermal expansion of electronic packaging components: a whole-field approach. IEEE Transactions on Components, Packaging, and Manufacturing Technology: Part A 19, 240–247.

Chen, H., 2025. Modeling and Control of Roll-to-roll Winding Machine in Li-ion Battery Manufacturing. Ph.D. thesis. University of Michigan.

Gelam, S.D., Maddipatla, S., Chicone, C., Pecht, M., 2024. Core collapse in cylindrical Li-ion batteries. Journal of Power Sources 623, 235471.

Gelam, S.D., Maddipatla, S., Chicone, C., Pecht, M., 2025. Anisotropic expansion-induced stress analysis of cylindrical Li-ion batteries. Journal of Power Sources 656, 238104.

Glock, D., 1977. Überkritisches Verhalten eines starr ummantelten Kreisrohres bei Wasserdruck von aussen und Temperaturdehnung. Der Stahlbau 46, 212–217. In German.

Jean, R.V., 1994. Phyllotaxis: A Systemic Study in Plant Morphogenesis. 1 ed., Cambridge University Press.

Kodio, O., Goriely, A., Vella, D., 2020. Dynamic buckling of an inextensible elastic ring: Linear and nonlinear analyses. Physical Review E 101, 053002.

Le, H.T., Haque, R.I., Ouyang, Z., Lee, S.W., Fried, S.I., Zhao, D., Qiu, M., Han, A., 2021. MEMS inductor fabrication and emerging applications in power electronics and neurotechnologies. Microsystems & Nanoengineering 7, 59.

Lee, C., 2018. Stresses and Defects in Roll Products: A Review of Stress Models and Control Techniques. International Journal of Precision Engineering and Manufacturing 19, 781–789.

Lee, C., Kang, H., Shin, K., 2012. Advanced taper tension method for the performance improvement of a roll-to-roll printing production line with a winding process. International Journal of Mechanical Sciences 59, 61–72.

Li, R., Li, W., Singh, A., Ren, D., Hou, Z., Ouyang, M., 2022. Effect of external pressure and internal stress on battery performance and lifespan. Energy Storage Materials 52, 395–429.

Mate, A., 2017. The frenet-serret formulas. Brooklyn Collage Of The City University Of New York, izdano 19.

Netz, R., 2017. On Spirals, in: The Works of Archimedes. 1 ed.. Cambridge University Press, pp. 17–180.

Noh, J., Jo, M., Kim, M., Lee, C., 2024. Advanced taper tension profile for improved control performance in roll-to-roll winding processes. Alexandria Engineering Journal 104, 279–291.

Omara, A., Guice, L., Straughan, W., Akl, F., 1997. Buckling models of thin circular pipes encased in rigid cavity. Journal of engineering mechanics 123, 1294–1301.

Palavesam, N., Marin, S., Hemmetzberger, D., Landesberger, C., Bock, K., Kutter, C., 2018. Roll-to-roll processing of film substrates for hybrid integrated flexible electronics. Flexible and Printed Electronics 3, 014002.

Peng, X., Meguid, S., 2017. Molecular dynamics simulations of the buckling behavior of defective carbon nanotubes embedded in epoxy nanocomposites. European Polymer Journal 93, 246–258.

Polezhaev, A., 2019. Spirals, Their Types and Peculiarities, in: Tsuji, K., Müller, S.C. (Eds.), Spirals and Vortices. Springer International Publishing, Cham, pp. 91–112. Series Title: The Frontiers Collection.

Putelat, T., Triantafyllidis, N., 2014. Dynamic stability of externally pressurized elastic rings subjected to high rates of loading. International Journal of Solids and Structures 51, 1–12.

Shi, X., Li, W., Min, J., Condon, A., Li, W., Attia, P.M., Zhu, J., 2026. Core Collapse Instability of Spirally Wound Jelly-Roll Lithium-Ion Batteries. Experimental Mechanics URL: https://link.springer.com/10.1007/s11340-026-01287-1, doi:10.1007/s11340-026-01287-1.

Timms, R., Psaltis, S., Please, C.P., Chapman, S.J., 2023. A mechanical model for reinforced, expanding spirally-wound layered materials. Journal of the Mechanics and Physics of Solids 175, 105269.

Timoshenko, S., Goodier, J., 1970. Theory of elasticity. McGraw-Hill, New York.

Timoshenko, S.P., Gere, J.M., 2012. Theory of elastic stability. Courier Corporation.

Wang, Z., Freris, N.M., Wei, X., 2025. SpiRobs: Logarithmic spiral-shaped robots for versatile grasping across scales. Device 3, 100646. URL: https://linkinghub.elsevier.com/retrieve/pii/S2666998624006033, doi:10.1016/j.device.2024.100646.

Wentworth Thompson, D., 1917. On growth and form Publisher: Cambridge University Press Cambridge.

Wierzbicki, T., Ling, J., 2024. Structural Mechanics: Bridging Theoretical Foundations and Real-World Disasters. 1 ed., CRC Press, Boca Raton. URL: https://www.taylorfrancis.com/books/9781003517146, doi:10.1201/9781003517146.

Yan, J., Zhang, X., Xu, B., Zhao, J., 2018. A New Spiral-Type Inflatable Pure Torsional Soft Actuator. Soft Robotics 5, 527–540. URL: https://journals.sagepub.com/doi/full/10.1089/soro.2017.0040, doi:10.1089/soro.2017.0040.

Zhu, J., Zhang, X., Sahraei, E., Wierzbicki, T., 2016. Deformation and failure mechanisms of 18650 battery cells under axial compression. Journal of Power Sources 336, 332–340.